JCNS811-01

Ghostbursting: A Novel Neuronal Burst Mechanism

Brent Doiron[*], Carlo Laing[*], André Longtin[*], and Leonard Maler[#]

[*]*Physics Department, University of Ottawa, 150 Louis Pasteur, Ottawa, Ontario, Canada K1N 6N5*

[#]*Department of Cellular and Molecular Medicine, University of Ottawa, 451 Smyth Road, Ottawa, Canada K1H 8M5*

Word Count Abstract: 225
Word Count Introduction: 1013
Word Count Discussion: 1844
Number of Text Pages: 28
Number of Figures: 13
Number of Tables: 1

Corresponding author:
Brent Doiron
Physics Department
University of Ottawa
Ottawa, Ontario
Canada K1N 6N5
Phone: (613) 562-5800 (8096)
FAX: (613) 562-5434
Email: bdoiron@physics.uottawa.ca

In Press, Journal of Computational Neuroscience

Keywords: bursting, electric fish, compartmental model, backpropagation, pyramidal cell

Abstract

Pyramidal cells in the electrosensory lateral line lobe (ELL) of weakly electric fish have been observed to produce high frequency burst discharge with constant depolarizing current (Turner et al., 1994). We present a two-compartment model of an ELL pyramidal cell that produces burst discharges similar to those seen in experiments. The burst mechanism involves a slowly changing interaction between the somatic and dendritic action potentials. Burst termination occurs when the trajectory of the system is reinjected in phase space near the "ghost" of a saddle-node bifurcation of fixed points. The burst trajectory reinjection is studied using quasi-static bifurcation theory which shows a period doubling transition in the fast subsystem as the cause of burst termination. As the applied depolarization is increased, the model exhibits first resting, then tonic firing, and finally chaotic bursting behaviour, in contrast with many other burst models. The transition between tonic firing and burst firing is due to a saddle-node bifurcation of limit cycles. Analysis of this bifurcation shows that the route to chaos in these neurons is type I intermittency, and we present experimental analysis of ELL pyramidal cell burst trains which support this model prediction. By varying parameters in a way that changes the positions of both saddle-node bifurcations in parameter space we produce a wide gallery of burst patterns, which span a significant range of burst time scales.

1 – Introduction

Burst discharge of action potentials is a distinct and complex class of neuron behaviour (Connors et al., 1982; McCormick et al., 1985; Connors and Gutnick, 1990). Burst responses show a large range of time scales and temporal patterns of activity. Many electrophysiological studies of cortical neurons have identified cells that intrinsically burst at low frequencies (<20 Hz) (Bland and Colom, 1993; Steriade et al., 1993; Franceschetti et al., 1995). However, recent work in numerous systems has now identified the existence of "chattering" cells which show burst patterns in the high frequency γ range (>20 Hz) (Turner et al., 1994; Paré et al., 1995; Gray and McCormick, 1996; Steriade et al., 1998; Lemon and Turner, 2000; Brumburg et al., 2000). Also, the specific inter-spike interval (ISI) pattern within the active phase of bursting varies considerably across burst cell types. Certain bursting cells show a lengthening of ISIs as a burst evolves (e.g. pancreatic-β cells, Sherman et al., 1990), others a parabolic trend in the ISI pattern (e.g *Aplysia* R15 neuron; Adams 1985), and yet others show no change in the ISI during a burst (e.g. thalamic reticular neuron; Pinault and Deschênes, 1992). This diversity of specific time scales and ISI patterns suggests that numerous distinct burst mechanisms exist. Knowledge of the burst mechanisms allows one to predict how the burst output may be modified, or halted completely in

response to stimuli. This may have consequences for the information content of the cell's output (Lisman, 1997).

Pyramidal cells in the electrosensory lateral line lobe (ELL) of the weakly electric fish *Apteronotus leptorhynchus* have been shown to produce either tonic firing and γ frequency sustained burst patterns of action potential discharge (Turner et al., 1994; Turner and Maler, 1999; Lemon and Turner, 2000). These secondary sensory neurons are responsible for transmitting information from populations of electroreceptor afferents that connect to their basal bushes (see Berman and Maler, 1999 and references therein). *In vivo* recordings from ELL pyramidal cells have indicated that their bursts are correlated with certain relevant stimulus features, suggesting the possible importance of ELL bursts for feature detection (Gabianni et al., 1996; Metzner and Gabianni, 1998; Gabianni and Metzner, 1999). Thus, both the proximity of ELL pyramidal cells to the sensory periphery, and the known relevance of their bursts to signal detection, suggest that studies of ELL bursting may provide novel results concerning the role of burst output in sensory processing.

Previous *in vitro* and *in vivo* experiments have focused both upon specifying the mechanism for burst discharge of ELL pyramidal cells, and showing methods for the modulation of burst output (Turner et al., 1994, 1996; Turner and Maler,1999; Lemon and Turner, 2000; Bastian and Nguyenkim, 2001; Rashid et al., 2001). Lemon and Turner (2000) have shown that a frequency dependent or "conditional" action potential backpropagation along the proximal apical dendrite underlies both the evolution and termination of ELL burst output. Recently, through the construction and analysis of a detailed multicompartmental model of an ELL pyramidal cell, we have reproduced burst discharges similar to those seen in experiment. This model allowed us to make strong predictions about the characteristics of the various ionic channels that could underlie the burst mechanism (Doiron et al., 2001b). However, a deeper understanding of the dynamics of the ELL burst mechanism could not be achieved due to the high dimensionality (312 compartments and 10 ionic currents) of the model system.

The analysis of bursting neurons using dynamical systems and bifurcation theory is well established (Rinzel, 1987; Rinzel and Ermentrout, 1989; Wang and Rinzel, 1995; Bertram et al., 1995; Hoppensteadt and Izhikevich, 1997; Izhikevich, 2000; Golubitsky et al., 2001). These studies have reduced complex neural behaviour to flows of low dimensional nonlinear dynamical systems. In the same spirit, we present here a two-compartment reduction of our detailed ionic

model of an ELL pyramidal cell (Doiron et al., 2001a, 2001b). The reduced model, referred to as the *ghostburster* (this term is explained in the text), produces burst discharges similar to both the full model and *in vitro* recordings of bursting ELL pyramidal cells. This analysis supports our previous predictions on the sufficient ionic and morphological requirements of the ELL pyramidal cell burst mechanism. In addition to this, the low dimension of this model allows for a detailed dynamical systems treatment of the burst mechanism.

When applied depolarization is treated as a bifurcation parameter, the model cell shows three distinct dynamical behaviours: resting with low intensity depolarizing current, tonic firing at intermediate levels, and chaotic burst discharge at high levels of depolarization. This is contrary to other burst mechanisms that show burst discharge for low levels of depolarization and then transition to tonic firing as applied current is increased (Hayashi and Ishizuka, 1992; Gray and McCormick, 1996; Steriade et al., 1998; Wang, 1999). Both of the bifurcations separating the three dynamical behaviours of the ghostburster are shown to be saddle-node bifurcations of either fixed points (quiescent to tonic firing) or limit cycles (tonic firing to bursting). Treating our burst model as a fast-slow burster (Rinzel, 1987; Rinzel and Ermentrout 1989, Wang and Rinzel, 1995; Izhikevich, 2000) and using quasi-static bifurcation analysis, we show that the burst termination is linked to a transition from period-one to period-two firing in the fast subsystem, causing the burst trajectory to be reinjected near the "ghost" of the saddle-node bifurcation of fixed points. The time spent near the saddle-node determines the inter-burst interval length.

This concept of burst discharge is quite different from the two-bifurcation analysis used to understand most other burst models (Rinzel, 1987; Rinzel and Ermentrout 1989,Wang and Rinzel, 1995; de Vries, 1998; Izhikevich, 2000; Golubitsky et al., 2001). Further analysis predicts that the route to chaos in transitioning from tonic to chaotic burst firing is through type I intermittency (Pomeau and Manneville, 1980). Comparisons of both model and experimental ELL burst recording data supports this prediction. Furthermore, by changing the relative position of the two saddle-node bifurcations in a two-parameter bifurcation set, the time scales of both the burst and inter-burst period can be chosen independently, allowing for wide variations in possible burst outputs.

2 – Methods

2.1 ELL pyramidal cell bursting

Figure 1*A* shows *in vitro* recordings from the soma of a bursting ELL pyramidal cell with a constant depolarizing input. The bursts comprise a sequence of action potentials, which appear on top of a slow depolarization of the subthreshold membrane potential. The depolarization causes the inter-spike-intervals (ISIs) to decrease as the burst evolves. The ISI decrease culminates in a high frequency spike doublet that triggers a relatively large after-hyperpolarization (AHP) labeled a burst-AHP (bAHP). The bAHP causes a long ISI that separates the train of action potentials into bursts, two of which are shown in Figure 1*A*. The full characterization of the burst sequence has been presented in Lemon and Turner (2000).

Immunohistochemical studies of the apical dendrites of ELL pyramidal cells have indicated a patched distribution of sodium channels along the first ~200 μm of the apical dendrite (Turner et al., 1994). Figure 1*B* illustrates schematically such a Na^+ channel distribution over the dendrite. The active dendritic Na^+ allows for action potential backpropagation along the apical dendrite, producing a dendritic spike response (Figure 1*B*; Turner et al., 1994). Na^+ or Ca^{2+} mediated action potential backpropagation has been observed in several other central neurons (Turner et al., 1994; Stuart and Sakmann, 1994; for a review of active dendrites see Stuart et al., 1997) and has been modeled in many studies (Traub et al., 1994; Mainen et al., 1995; Vetter et al., 2001; Doiron et al., 2001b). Action potential backpropagation produces a somatic depolarizing after-potential (DAP) after the somatic spike, as shown in Figure 1*B*. The DAP is the result of a dendritic reflection of the somatic action potential. This requires both a long dendritic action potential half-width as compared to that of a somatic action potential, and a large somatic hyperpolarization succeeding an action potential. These two features allow for passive electrotonic current flow from the dendrite to the soma subsequent to the somatic spike, yielding a DAP.

Recent work has shown the necessity of spike backpropagation in ELL pyramidal cells for burst discharge (Turner et al., 1994; Turner and Maler, 1999; Lemon and Turner, 2000). These studies blocked spike backpropagation by locally applying tetrodoxin (TTX, a Na^+ channel blocker) to apical dendrites of ELL pyramidal cells, after which all bursting ceased and only tonic firing persisted. Our previous modeling study (Doiron et al., 2001b), reproduced this result, since when active Na^+ conductances were removed from all dendritic compartments, similar results were

obtained. However, in that study we modeled the proximal apical dendrite with ten compartments, five of which contained active spiking Na^+ channels. The large number of variables in such a model is incompatible with the objectives of the present study. In light of this, and following previous modeling studies involving action potential backpropagation (Pinsky and Rinzel, 1994; Bressloff, 1995; Mainen and Sejnowski, 1996; Lánsky and Rodriguez, 1999; Wang, 1999; Booth and Bose, 2001), we investigate a two-compartment model of an ELL pyramidal cell, where one compartment represents the somatic region, and the second the entire proximal apical dendrite. Note that a two-compartment treatment of dendritic action potential backpropagation is a simplification of the cable equation (Keener and Sneyd, 1998). However, in consideration of the goals of the present study, which require only DAP production, the two-compartment assumption is sufficient.

2.2 Two-Compartment Model

A schematic of our two-compartment model of an ELL pyramidal cell is shown in Figure 2, together with the active inward and outward currents that determine the compartment membrane potentials. Both the soma and dendrite contain fast inward Na^+ currents, $I_{Na,s}$ and $I_{Na,d}$, and outward delayed rectifying (Dr) K^+ currents, respectively $I_{Dr,s}$ and $I_{Dr,d}$. These currents are necessary to reproduce somatic action potentials, and proper spike backpropagation that yields somatic DAPs. In addition, both the soma and dendrite contain passive leak currents I_{leak}. The membrane potentials V_s (somatic) and V_d (dendritic) are determined through a modified Hodgkin/Huxley (1952) treatment of each compartment. The coupling between the compartments is assumed to be through simple electrotonic diffusion giving currents from soma to dendrite , $I_{s/d}$, or vice-versa, $I_{d/s}$. In total, the dynamical system comprises six nonlinear differential equations, Eq (1)-(6); henceforth, we will refer to Eq(1)-(6) as the *ghostburster* model, and the justification for the name will be presented in the Results section.

Soma

$$(1)\quad \frac{dV_s}{dt} = I_S + g_{Na,s}\cdot m_{\infty,s}{}^2(V_s)\ \cdot(1-n_s)\cdot(V_{Na}-V_s) + g_{Dr,s}\cdot n_s{}^2\cdot(V_K-V_s) + \frac{g_c}{\boldsymbol{k}}\cdot(V_d-V_s) + g_{leak}\cdot(V_l-V_s)$$

$$(2)\quad \frac{dn_s}{dt} = \frac{n_{\infty,s}(V_s)-n_s}{\boldsymbol{t}_{n,s}}$$

Dendrite

$$(3)\quad \frac{dV_d}{dt} = g_{Na,d}\cdot m_{\infty,d}{}^2(V_d)\ \cdot h_d\cdot(V_{Na}-V_d) + g_{Dr,d}\cdot n_d{}^2\cdot p_d\cdot(V_K-V_d) + \frac{g_c}{(1-\boldsymbol{k})}\cdot(V_s-V_d) + g_{leak}\cdot(V_l-V_d)$$

$$(4)\quad \frac{dh_d}{dt} = \frac{h_{\infty,d}(V_d)-h_d}{\boldsymbol{t}_{h,d}}$$

$$(5)\quad \frac{dn_d}{dt} = \frac{n_{\infty,d}(V_d)-n_d}{\boldsymbol{t}_{n,d}}$$

$$(6)\quad \frac{dp_d}{dt} = \frac{p_{\infty,d}(V_d)-p_d}{\boldsymbol{t}_{p,d}}$$

Table I lists the values of all channel parameters used in the simulations. The soma is modeled with two variables (see eq. (1) and (2)). The reduction from the classic four dimensional Hodgkin-Huxley model is accomplished by slaving $I_{Na,s}$ activation, $m_{\infty,s}$, to V_s (i.e the Na^+ activation m_s tracks V_s instantaneously), and modeling its inactivation ,h_s, through $I_{Dr,s}$ activation, n_s (we set $h_s \equiv 1-n_s$). This second approximation is a result of observing in our large compartmental model (Doiron et al., 2001b) that $h_s + n_s \approx 1$ during spiking behaviour. Both of these approximations

have been used in various other models of spiking neurons (Keener and Sneyd, 1998). The dendrite is modeled with four variables (see eq. (3)-(6)). Similar to the treatment of $I_{Na,s}$, we slave $I_{Na,d}$ activation, $m_{\infty,d}$, to V_d, but model its inactivation with a separate dynamical variable h_d. Lemon and Turner (2000) have shown that the refractory period of dendritic action potentials is larger than that of somatic in ELL pyramidal neurons. This result has previously been shown to be necessary for burst termination (Doiron et al., 2001b). To model differential somatic/dendritic refractory period we have chosen $\tau_{h,d}$ to be longer than $\tau_{n,s}$ (similar to our large compartmental model (Doiron et al., 2001b)). This result has not been directly verified through immunohistochemical experiments of ELL pyramidal cells Na^+ channels, thus, at present, this remains an assumption in our model.

The crucial element for the success of our model in reproducing bursts is the treatment of $I_{Dr,d}$. Dendritic recordings from bursting ELL pyramidal cells show a slow, frequency dependent broadening of the action potential width as a burst evolves (Lemon and Turner, 2000). Such a cumulative increase in action potential width has been observed in other experimental preparations, and has been linked to a slow inactivation of rectifier-like K^+ channels (Aldrich et al., 1979; Ma and Koester, 1996; Shao et al., 1999). In light of this, our previous study (Doiron et al., 2001b), modeled the dendritic K^+ responsible for spike rectification with both activation and inactivation variables. When the time constant governing the inactivation was relatively long (5 ms) compared with the time constants of the spiking currents (~ 1ms), the model produced a burst discharge comparable to ELL pyramidal cell burst recordings. Doiron et al. (2001b) also considered other potential burst mechanisms, including slow activation of persistent sodium, however, only slow inactivation of dendritic K^+ produced burst results comparable to experiment. At this time there is no direct evidence for a cumulative inactivation of dendritic K^+ channels in ELL pyramidal cells, and these results remain a model assumption. However, preliminary work suggests that the *shaw*-like *Apt*Kv3.3 channels may express such a slow inactivation (R.W. Turner personal communication); these channels have been shown to be highly expressed in the apical dendrites of ELL pyramidal cells (Rashid et al., 2001). In the present work, our dynamical system also models dendritic K^+ current, $I_{Dr,d,}$ as having both activation, n_d, and slow inactivation p_d variables (see Eqs. (3),(5), and (6)). Slow inactivation of K^+ channels, although not a mechanism in contemporary burst models, was proposed by Carpenter (1979), in the early stages of mathematical treatment of bursting in excitable cells. We do not implement a similar slow

inactivation of somatic Dr,s since somatic spikes observed in bursting ELL pyramidal cells do not exhibit broadening as the burst evolves (Lemon and Turner, 2000).

The somatic-dendritic interaction is modeled as simple electrotonic diffusion with coupling coefficient g_c, and scaled by the ratio of somatic-to-total surface area κ. This form of coupling has been used in previous two-compartment neural models (Mainen and Sejnowski, 1996; Wang 1999; Kepecs and Wang, 2000; Booth and Bose, 2001). I_S represents either an applied or synaptic current flowing into the somatic compartment. In the present study I_S is always constant in time, and will be used as a bifurcation parameter. Physiological justification for the parameter values given in Table I is presented in detail in Doiron et al. (2001b). Eqs (1) – (6) are integrated by a 4^{th} order Runge-Kutta algorithm with a fixed time step of $\Delta t=5\times10^{-6}$ s.

3 – Results

3.1 Model performance

Figure 3*A* and 3*B* show simulation time series of V_s and p_d, respectively, for the ghostburster with constant depolarization of $I_S = 9$. We see a repetitive burst train similar to that shown in Figure 1*A*. Figure 4 compares the time series of V_s and V_d for the ghostburster (bottom row) during a single burst, to both a somatic and dendritic burst from ELL pyramidal cell recordings (top row), and the large compartmental model presented in Doiron et al., (2001b) (middle row). All burst sequences are produced with constant somatic depolarization. The somatic bursts all show the same characteristic growth in depolarization (DAP growth), and consequent decreases in ISI leading to the high frequency doublet. The dendritic bursts all show that a dendritic spike failure is associated with both doublet spiking and burst termination. The somatic AHPs in the simulation of the ghostburster do not show a gradual depolarization during the burst, as do both the AHPs in the ELL pyramidal cell recordings and the large compartmental model simulations. This is a minor discrepancy, which is not relevant for the understanding of the burst mechanism.

The mechanism involved in the burst sequences shown in Figures 3 and 4 has been explained in detail (although not from a dynamical systems point of view) in past experimental and computational studies (Lemon and Turner, 2000; Doiron et al., 2001b). We give a short overview of this explanation. Action potential backpropagation is the process of a somatic action potential actively propagating along the dendrite due to activation of dendritic Na^+ cahnnels. Rapid

hyperpolarization of the somatic membrane, mediated by somatic potassium activation n_s, allows electrotonic diffusion of the dendritic action potential, creating a DAP in the somatic compartment. However, with repetitive spiking the dendritic action potentials, shown by V_d, broaden in width and show a baseline summation (Figure 4). This is due to the slow inactivation of $I_{Dr,d}$, mediated by p_d, as shown in Figure 3*B*. This further drives electrotonic diffusion of the dendritic action potential back to the soma; consequently, the DAP at the soma grows, producing an increased somatic depolarization as the burst evolves. This results in decreasing somatic ISIs, as experimentally observed during ELL burst output. This positive feedback loop between the soma and dendrite finally produces a high frequency spike doublet (Figure 4).

Doublet ISIs are within the refractory period of dendritic spikes but not that of somatic spikes (Lemon and Turner, 2000). This causes the backpropagation of the second somatic spike in the doublet to fail, due to lack of recovery of $I_{Na,d}$ from its inactivation, as shown in the dendritic recordings (Figure 4). This backpropagation failure removes any DAP at the soma, uncovering a large bAHP, and thus terminates the burst. This creates a long ISI, the inter-burst period, which allows p_d and h_d to recover, in preparation for the next burst (see Figure 3*B*).

3.2 Bifurcation Analysis

In the following sections we will use dynamical systems theory to explore various aspects of the ghostburster equations (Eq. (1)-(6)). An introduction to some of the concepts we will use can be found for example in Strogatz (1994). An alternative explanation of the burst mechanism, given in physiological terms, was presented in Doiron et al. (2001b).

Figure 5*A* gives the bifurcation diagram of h_d as computed from the ghostburster with I_S treated as the bifurcation parameter. We chose I_S since this is both an experimentally and physiologically relevant parameter to vary. Three distinct dynamical behaviours are observed. For $I_S < I_{S1}$ two fixed points exist; one stable, representing the resting state, and one unstable saddle. When $I_S = I_{S1}$ the stable and unstable fixed points coalesce in a saddle-node bifurcation of fixed points on an invariant circle, after which a stable limit cycle exists. This is characteristic of Class I spike excitability (Ermentrout, 1996), of which the canonical model is the well-studied θ neuron (Hoppensteadt and Izhikevich, 1997). For $I_{S1} < I_S < I_{S2}$ the stable limit cycle coexists with an unstable limit cycle. Both limit cycles coalesce at $I_S = I_{S2}$ in a saddle-node bifurcation of limit cycles. For $I_S > I_{S2}$ the model dynamics, lacking any stable periodic limit cycle, evolve on a chaotic attractor giving bursting solutions as shown in Figures 3 and 4 (lower panel). As I_S

increases further a period doubling cascade out of chaos is observed, and a period two solution exists for high I_S. The importance of both of the saddle-node bifurcations will be explored in later sections.

Figure 5*B* shows the observed spike discharge frequencies, f ($\equiv$1/ISI), from the ghostburster as I_S is varied over the same range as in Figure 5*A*. The rest state, $I_S < I_{S1}$, admits no firing, indicated by setting f = 0. For $I_{S1} < I_S < I_{S2}$ the stable limit cycle attractor produces repetitive spike discharge giving a single nonzero f value for each value of I_S. f becomes arbitrarily small as I_S approaches I_{S1} from above due to the infinite period bifurcation at I_{S1}. However, for $I_S > I_{S2}$ the attractor produces a varied ISI pattern, as shown in Figures 3 and 4. This involves a range of observed f values for a given fixed I_S, ranging from ~ 100 Hz in the inter-burst interval to almost 700 Hz at the doublet firing. The burst regime, $I_S > I_{S2}$ does admit windows of periodic behaviour. A particularly large window of $I_S \in$ (13.13,13.73) shows a stable period six solution which undergoes a period doubling cascade into chaos as I_S is decreased. Finally, the period doubling cascade out of chaos for $I_S >> I_{S2}$ is evident.

Figure 5*C* shows the most positive Lyapunov exponent, λ, of the ghostburster as a function of I_S. We see that $\lambda < 0$ for $I_S < I_{S1}$ because the only attractor is a stable fixed point. For $I_{S1} < I_S < I_{S2}$, $\lambda = 0$ because the attractor is a stable limit cycle. Of particular interest is that λ is positive for a range of I_S greater than I_{S2}, indicating that the bursting is chaotic. The windows of periodic behaviour within the chaotic bursting are indicated by λ being zero (e.g. the large window for $I_S \in$ (13.13,13.73)). For $I_S > 17.65$, $\lambda = 0$ because the ghostburster undergoes a period doubling cascade out of chaos, resulting in a stable period two solution.

Figure 6 is a two parameter bifurcation set showing curves for both the saddle-node bifurcation of fixed points (SNFP) and of limit cycles (SNLC). The parameters are the applied current I_S, already studied in Figure 5, and $g_{Dr,d}$ which controls the influence of the slow dynamical variable p_d (see Eq (3)). It is natural to choose $g_{Dr,d}$ as the second bifurcation parameter since the burst mechanism involves dendritic backpropagation, which $I_{Dr,d}$ regulates, and $g_{Dr,d}$ can be experimentally adjusted by focal application of K^+ channel blockers to the apical dendrites of ELL pyramidal cells (Rashid et al., 2001). A vertical line in Figure 6 corresponds to a bifurcation diagram similar to that presented in Figure 5*A*. The diagram in Figure 5*A* corresponds to the rightmost value of $g_{Dr,d}$ in Figure 6 ($g_{Dr,d}$ =15). The intersection of the curves SNFP and SNLC with any vertical line gives the values I_{S1} and I_{S2} for that particular value of $g_{Dr,d}$. Thus, the curves

SNFP and SNLC partition parameter space into regions corresponding to quiescence, tonic firing, and chaotic bursting solutions of the ghostburster equations, as indicated in Figure 6. The curves intersect at a codimension-two bifurcation point corresponding to simultaneous fixed point and limit cycle saddle-node bifurcations. The curve to the left of the intersection point corresponds to the codimension one SNFP curve; there is no stable period-one limit cycle corresponding to tonic firing in this region. Figure 6 demonstrates that it is possible to make I_{S1} and I_{S2} arbitrarily close, by choosing $g_{Dr,d}$ appropriately. This property will be of use later in the study.

3.3 The Burst Mechanism : Reconstructing the Burst Attractor.

The dynamical system described by the ghostburster equations possesses two separate time scales. The time constants governing the active ionic channels n_s, h_d, and n_d, are all ~ 1 ms, and the half width of the spike response of the membrane potentials V_s and V_d are ~ 0.5 ms and 1.1 ms respectively. However, the time scale of p_d is characterized by $\tau_{p,d}$, which is a factor of five times larger than any of the other time scales. Previous studies of other burst models have profited from a similar coexistence of at least two time scales of activity during bursting (Rinzel, 1987; Rinzel and Ermentrout, 1989; Wang and Rinzel, 1995; Bertram et al., 1995; de Vries, 1998; Izhikevich, 2000; Golubitsky et al., 2001). This allowed for a separation of the full dynamical system into two smaller subsystems, one fast and one slow. We also treat our burst model as a fast-slow burster. The natural variable separation is to group V_s, n_s, V_d, h_d, and n_d into a fast subsystem, denoted by the vector x, while the slow subsystem consists solely of p_d. This gives the simplified notation of our model,

$$\frac{dx}{dt} = f(x, p_d) \tag{7}$$

$$\frac{dp_d}{dt} = \frac{p_{d,\infty}(x) - p_d}{\tau_{p,d}} \tag{8}$$

where $f(x,p_d)$ represents the right hand side of Eqs. (1)-(5) and Eq. (8) is simply Eq (6) restated.

Since p_d changes on a slower time scale than x, we approximate p_d as constant, and use p_d as a bifurcation parameter of the fast subsystem (quasi-static approximation; see e.g. Hoppensteadt and Izhikevich, 1997). We note that with p_d constant the fast subsystem (7) cannot produce bursting comparable to that seen from ELL pyramidal cells. Bursting requires the slow variable to modulate DAP growth dynamically (Doiron et al., 2001b). Treating p_d as a bifurcation parameter

will show how changes in p_d produce the characteristics of ELL bursting through the bifurcation structure of the fast subsystem. Since p_d only directly affects the fast subsystem through the dynamics of V_d (see eq. (3)) we choose V_d as a representative variable of the fast subsystem x.

Figure 7*A* shows the local maxima of V_d on a periodic orbit as a function of p_d, while the fast subsystem is driven with $I_S = 9 > I_{S2}$. At a critical value of p_d, labeled p_{d1}, the fast subsystem goes through a transition from a period-one to a period- two limit cycle. This is shown by only one maximum in V_d for $p_d > p_{d1}$, whereas there are two maxima for $p_d < p_{d1}$. Figure 7*B* shows a time series of $V_d(t)$ following the period-one limit cycle when $p_d = 0.13 > p_{d1}$, while Figure 7C shows the period-two limit cycle when $p_d = 0.08 < p_{d1}$. The second dendritic action potential in the period-two orbit (Figure 7*C*) is of reduced amplitude; this corresponds to the dendritic failure observed in the full dynamical system (Eqs (7) and (8)) when p_d is low (see right column of Figure 4). The bifurcation diagram in Figure 7*A* may be thought of as a "burst shell" in a projection of phase space. The full burst dynamics will evolve upon the burst shell as p_d is modulated slowly by the fast subsystem. We therefore next address the dynamics of $p_d(t)$ during the burst trajectory in the fast subsystem.

Upon inspection of Figure 3*B* it is clear that there exists two oscillations in $p_d(t)$, one fast oscillation occurring on the time scale of spikes, and the other on a much longer time scale, tracking the bursts. Figure 8 shows $p_d(t)$ during a burst solution of the full dynamical system. It is clear that the fast spike oscillations in $p_d(t)$ are driven by the instantaneous value of $V_d(t)$. This is due to τ_p being small enough to allow $p_d(t)$ to be affected by the spiking in the fast subsystem. In addition, there is a general decrease in $p_d(t)$ as the burst evolves, and an sharp increase in $p_d(t)$ after the doublet ISI. The increase reinjects $p_d(t)$ to a higher value allowing the burst oscillation to begin again. The period of a burst oscillation encompasses several spikes, and thus cannot be analyzed in terms of the instantaneous dynamics of the fast subsystem.

Due to the separation of time scales, and the fact that dp_d/dt depends only on V_d (eq. (6)), we expect that the burst oscillation depends on the average of V_d between consecutive spikes, defined as

$$(9) \quad \langle V_d \rangle = \frac{1}{t_{i+1} - t_i} \int_{t_i}^{t_{i+1}} V_d(t) dt$$

where t_i is the time of the i_{th} spike. We construct a discrete function $\tilde{p}_d$

(10) $\tilde{p}_d = p_{d,\infty}(\langle V_d \rangle)$

where $p_{d,\infty}(\cdot)$ is the infinite conductance curve as in eq. (6). Figure 8 shows a sequence of $\tilde{p}_d$ values constructed by using $\langle V_d \rangle$ from the burst solution of the full dynamical system. This sequence is plotted (solid circles) on top of the full p_d(t) dynamics during the burst train. It is evident that the time sequence of $\tilde{p}_d$ is of the same shape as the burst oscillation in p_d(t). This is evidence that the slow burst oscillation can be analyzed by considering $\langle V_d \rangle$.

We now complete the burst shell by adding to Figure 7*A* the nullcline for p_d (from eq. (6)) as well as $\langle V_d \rangle$ computed for the stable periodic solutions of the fast subsystem. This is shown in Figure 9*A*. Note that as p_d decreases through p_{d1}, $\langle V_d \rangle$ decreases by ~10 mV. This is due to the dendritic spike failure and subsequent long ISI occurring when $p_d < p_{d1}$, both contributing to lower V_d on average (see Figure 7*C*). The p_d nullcline and $\langle V_d \rangle$ curves cross at $p_d = p_{d2} < p_{d1}$. Since we have shown that the burst oscillation is sensitive to $\langle V_d \rangle$, the crossing corresponds to $\left\langle dp_d/dt \right\rangle$ changing from negative to positive (see Figure 9*D*).

A saddle-node bifurcation of fixed points occurs at $p_d = p_d^*$ for some $p_d^* > p_{d1}$ (data not shown). This bifurcation is similar to the saddle-node bifurcation of fixed points in Figure 5*A*, where I_S is the bifurcation parameter. This is expected, since p_d is the coefficient to a hyperpolarizing ionic current (see eq. (3)), hence an increase in p_d is equivalent to a decrease in depolarizing I_S. Because of the saddle-node bifurcation at $p_d = p_d^*$, the period of the period-one limit cycle scales as $1/\sqrt{|p_d - p_d^*|}$ for p_d near p_d^* (Guckenheimer and Holmes, 1983).

With the burst shell now fully constructed (Figure 9*A*) we place the full burst dynamics (eq. (7)-(8)) onto the shell. This is shown in Figure 9*B*. The directed trajectory is the full six dimensional burst trajectory projected into the V_d - p_d subspace. As the burst evolves, p_d(t) decreases from spike to spike in the burst. This causes the frequency of spike discharge to increase due to the gradual shift away from the saddle-node bifurcation of fixed points at $p_d = p_d^*$. However, once p_d(t) < p_{d1} the spike dynamics shift from period-one spiking to period-two spiking. This first produces a high frequency spike doublet, which is then followed by a dendritic potential

of reduced amplitude, causing $\langle V_d \rangle$ to decrease. When $p_d(t) < p_{d2}$, $\left\langle dp_d/dt \right\rangle > 0$ (see Figure 8*D*), and $p_d(t)$ increases and is reinjected to a higher value. *The reinjection towards the " ghost" of the saddle-node bifurcation of fixed points causes the ISI (the inter-burst interval) to be long, since the velocity through phase space is lower in this region.*

Figure 9*C* shows the burst trajectory in the frequency domain. The period doubling is evident at $p_d = p_{d1}$ since two distinct frequencies are observed for $p_d < p_{d1}$, corresponding to a period two solution of the fast subsystem, whereas for $p_d > p_{d1}$ only a period one solution is found. As p_d is reduced in the period one regime ($p_d > p_{d1}$) the frequency of the limit cycle increases, due to the reduced effect of the hyperpolarizing current $I_{Dr,d}$. We superimpose the ISIs of the burst trajectory shown in Figure 9*B* on the frequency bifurcation diagram in Figure 9*C*. The sequence begins with a long ISI (numbered 1) with subsequent ISIs decreasing, culminating with the short doublet ISI (numbered 5). The reinjection of p_d near p_d^* occurs during the next ISI (numbered 6). The reinjection causes this next ISI to be long; it separates the action potentials into bursts. Figure 9*D* shows the average of the derivative of p_d, $\left\langle dp_d/dt \right\rangle = \frac{1}{t_{i+1} - t_i} \int_{t_i}^{t_{i+1}} \left(dp_d/dt \right) dt$, during each ISI in the burst shown in Figures 9*B*, and 9*C*. Notice that $\left\langle dp_d/dt \right\rangle$ is negative and decreases as the burst evolves. This is because the ISI length reduces as the burst evolves, allowing the burst trajectory to spend less time in the region where $dp_d/dt > 0$. However, a large fraction of the burst trajectory during the inter-burst ISI (6) occurs in the region where $dp_d/dt > 0$. Hence, the average $\left\langle dp_d/dt \right\rangle$ is greater than zero for the inter-burst interval, producing the reinjection of $p_d(t)$ to higher values.

Izhikevich (2000) has labeled the burst mechanisms according to the bifurcations in the fast subsystem that occur in the transition from quiescence to limit cycle and vice versa. Even though there is never a true "quiescent" period during the burst phase trajectory, the inter-burst interval for our model is determined by the approach to an infinite period bifurcation. This phenomenon is often labeled as sensing the "ghost" of a bifurcation (Strogatz, 1994), and we naturally label the burst mechanism as *ghostbursting*.

The ghostburster system exhibits bursting, for some range of I_S, only for $2 < \tau_p < 110$ ms, with all other parameters as given in Table 1. The lower bound of τ_p is due to the fact that the inactivation of $I_{Dr,d}$ must be cumulative in order for there to be a reduction of the ISIs as the burst evolves. This requires a τ_p larger than that of the ionic channels responsible for spike production (< 1 ms). The upper bound on τ_p is also expected since significant removal of p_d inactivation during the inter-burst interval is necessary for another burst to occur. Too large a value of τ_p will not allow sufficient recovery of $I_{Dr,d}$ from inactivation and therefore bursting will not occur.

3.4- The Inter-burst Interval.

By varying I_S it is possible to set the inter-burst interval, T_{IB}, to be different lengths. This is because after the dendrite has failed (removing the DAP at the soma) the time required to produce an action potential in the somatic compartment (which is T_{IB}) is dictated almost solely by I_S. The spike excitability of the somatic compartment is Type I (Ermentrout, 1996), as evident from the saddle-node bifurcation of fixed points at $I_S = I_{S1}$. As a consequence T_{IB} is determined from the well-known scaling law associated with saddle-node bifurcations on a circle (Guckenheimer and Holmes, 1983),

$$T_{IB} \sim 1/\sqrt{I_S - I_{S1}}. \qquad (11)$$

Figure 10 shows the average inter-burst interval, $\langle T_{IB} \rangle$, as a function of $I_S - I_{S1}$ for the ghostburster with $g_{Dr,d} = 12.14$. This value of $g_{Dr,d}$ sets I_{S1} and I_{S2} close to one another (see Figure 6), allowing the system to burst with values of I_S close to I_{S1}. It is necessary to form an average due to the chaotic nature of burst solutions. Nevertheless, $\langle T_{IB} \rangle$ increases as I_S approaches I_{S1}, as suggested by Eq. (11). A linear regression fit of $1/\langle T_B \rangle^2$ against $I_S - I_{S1}$ gives a correlation coefficient of 0.845 further verifying that Eq (11) holds. Figure 10 also shows downward dips in $\langle T_{IB} \rangle$ that occur more frequently as $I_S - I_{S1}$ goes to zero. Time series of bursts with I_S corresponding to the dips in $\langle T_{IB} \rangle$ show scattered bursts with short inter-burst intervals that deviate from Eq (11), amongst bursts with longer inter-burst intervals, which fit the trend described by Eq (11). These scattered small values of T_{IB} reduce $\langle T_{IB} \rangle$ for these particular values of I_S. These dips contribute to the deviation of the linear correlation coefficient cited above from 1. We do not study the dips further since the behaviour has yet to be observed experimentally. However, experimental measurements of ELL pyramidal cell burst period do indeed show a lengthening of the period as

the applied current is reduced (R.W. Turner, personal communication). This corresponds to the general trend shown in Figure 10. Eq (11) and Figure 10 show that by choosing the model parameters properly it is possible to regulate the effect of the ghost of the saddle-node bifurcation of fixed points on the burst solutions. We will show later how this property yields great diversity of time scales of possible burst solutions of the ghostburster model.

3.5- The Burst Interval – Intermittency.

Regions of chaotic and periodic behaviour exist in many burst models (Chay and Rinzel, 1985; Terman, 1991; Terman, 1992; Hayashi and Ishizuka, 1992; Wang, 1993; Komendantov and Kononenko, 1998). The results of Figure 5 show that periodic spiking and chaotic bursting are also two distinct dynamical behaviours of the ghostburster. Moreover, the bifurcation parameter we have used to move between both dynamical regimes is the applied current I_S which mimics an average synaptic input to the cell. This indicates that changing the magnitude of input to the cell may cause a transition from periodic spiking to chaotic bursting. In ELL pyramidal cells a transition from tonic firing to highly variable bursting has been observed as applied depolarizing current is increased (Lemon and Turner, 2000; Bastian and Nguyenkim, 2001; Doiron and Turner, unpublished results). It remains to be shown that the experimentally observed bursting is indeed chaotic; preliminary results suggest that such an analysis is difficult due to non-stationarity in the data (Doiron and Turner, unpublished observations). Nonetheless, understanding the transitions or routes to chaos in the model separating tonic and chaotic burst regimes is not only necessary for a complete description of the dynamics of the model, but also for characterizing the input-output relation of bursting ELL pyramidal cells.

Figure 5*A* shows that the transition from periodic spiking to chaotic bursting occurs at $I_S=I_{S2}$ when a stable limit cycle collides with an unstable periodic orbit in a saddle-node bifurcation of limit cycles. Since we are analyzing spiking behaviour on both sides of the bifurcation it is natural to consider the ISI return map for I_S near I_{S2}. We choose I_S slightly larger than I_{S2} and plot in Figure 11*A* the ISI return map for a single burst sequence from the ghostburster (for $I_{S1}<I_S<I_{S2}$ the return map is a single point). We have labeled the regions of interest in the Figure and explain each region in order: (1) The burst begins here. (2) The ISI sequence approaches the diagonal. This produces a clustering of points corresponding to the pseudo-periodic behaviour observed in the center of the burst. We refer to this region of the map as a *trapping* region. (3) The ISI

sequence leaves the trapping region with a downward trend. (4) The inter-burst interval involves a sharp transition from small ISI to large ISI. (5) The ISI sequence returns to the trapping region and another burst begins.

The above description indicates that the route to chaos is Type I intermittency (Manneville and Pomeau, 1980; Guckenheimer and Holmes, 1983). Intermittency involves seemingly periodic behaviour separated by brief excursions in phase space. The clustering of points in the ISI return map in the trapping region of Figure 11*A* (labeled 2) is a manifestation of this apparent periodic firing. A trapping region is a characteristic feature of Type I intermittency and corresponds to a saddle-node bifurcation of limit cycles in the return map, occurring specifically at $I_S=I_{S2}$ for the ghostburster equations. The escape and return to the trapping region (regions 3,4,5 in Figure 11*A*) are the brief excursions. These events correspond to the period doubling transition and the cross of the $\langle V_d \rangle$ curve and p_d nullcline, in the fast subsystem, as explained in Figure 9. Figure 11*B* shows the ISI return map for a model burst of seven spikes and Figure 11*C* the same map for a seven spike burst recording from an ELL pyramidal cell. Both maps show the qualitative structure similar to in Figure 11*A*, including a clear escape from and reinjection into a trapping region near the diagonal. Interestingly, Wang (1993) has also observed Type I intermittency in the Hindmarsh-Rose model).

Since intermittent behaviour is connected to a saddle-node bifurcation, the time spent in the trapping region T_B, corresponding to the burst period (the duration of the spikes in the cluster making up the burst), has a well defined scaling law

$$(12) \quad T_B \sim \frac{1}{\sqrt{I_S - I_{S2}}}$$

Similar to Figure 10 we consider the average of the burst period, $\langle T_B \rangle$, because of the chaotic nature of the bursting. Figure 12 shows that $\langle T_B \rangle$ asymptotes to infinity as I_S approaches I_{S2}. Linear regression fits to $1/\langle T_B \rangle^2$ against $I_S - I_{S2}$ give a correlation coefficient of 0.886. These results validate Eq (12) for the ghostburster burst sequences. Again the deviation in the correlation coefficient from 1 is caused by slight dips in $\langle T_B \rangle$, similar to the dips observed in $\langle T_{IB} \rangle$ (Figure 10). By choosing the quantity I_S-I_{S2} we can obtain bursts with spike numbers comparable to experiment.

3.6 - Gallery of Bursts

Eqs (11) and (12) give the inverse square root scaling relations of T_B and T_{IB} respectively. These results showed that T_B is determined by I_S-I_{S2} and T_{IB} by I_S-I_{S1}. Using this fact and the ability to vary the difference between I_{S2} and I_{S1} (see Figure 6) we can produce a wide array of burst patterns with differing time scales.

Figure 13A reproduces the (I_S , $g_{Dr,d}$) bifurcation set shown in Figure 6. The letters B-F mark (I_S , $g_{Dr,d}$) parameters used to produce the spike trains shown in the associated panels B-F of Figure 13. Figure 13*B* uses (I_S , $g_{Dr,d}$) values such that the ghostburster is in the tonic firing regime. The burst trains shown in Figures 3 and 4 correspond to (I_S , $g_{Dr,d}$) values in the burst regime of Figure 6 which are not close to either of the SNFP or SNLC curves. An example of a burst train with such a parameter choice, is shown in Figure 13*C*. However, if we approach the SNLC curve but remain distant from the SNFP curve, we can increase T_B by one order of magnitude yet keep T_{IB} the same. The burst train in Figure 13D shows an example of this. If we choose I_S and $g_{Dr,d}$ to be close to both the SNFP and SNLC curves we can now increase T_{IB} as well (Figure 13*E*). The inter-burst period T_{IB} has now also increased dramatically from that shown in Figures 13*C* and *D*.

Finally, for I_S and $g_{Dr,d}$ values to the left of the codimension two bifurcation point, burst sequences show only a period two solution (Figure 13*F*). The burst sequences are no longer chaotic. This is to be expected since there no longer is a saddle-node bifurcation of limit cycles, which gave rise to the intermittency route to chaos in the ghostburster equations (Figure 11). Approaching the SNFP curve allows for a large T_{IB}, but the fact that only bursts of two spikes can appear forces T_B to be small. The restriction of bursts to only doublets when $g_{Dr,d}$ is small occurs because $g_{Dr,d}$ is the coefficient to the hyperpolarizing K^+ current in the dendrite (Eq (3)), and as such controls the effect of the DAP at the soma. For $g_{Dr,d}$ to the left of the codimension-two bifurcation point, the first somatic spike in the doublet produces a DAP of sufficient strength to cause the second somatic spike which is within the refractory period of the dendrite. Thus dendritic failure occurs after the first reflection and the burst contains only two spikes.

4 – Discussion

4.1 Ghostbursting: a Novel Burst Mechanism

We have introduced a two-compartment model of bursting ELL pyramidal cells, titled the ghostburster. The model is a significant reduction of a large multi-compartmental ionic model of these cells (Doiron et al., 2001b). The large model was motivated by the 'conditional' backpropagation burst mechanism that has been experimentally characterized in ELL pyramidal cells (Lemon and Turner, 2000). The results of Lemon and Turner (2000) and Doiron et al., (2001b), suggest that the ionic requirements necessary and sufficient to support bursting as observed in the ELL are 1) action potential backpropagation along the apical dendrite sufficient to produce somatic DAPs. 2) the refractory period of dendritic action potentials must be longer than that of the somatic potentials 3) slow inactivation of a dendritic K^+ channel involved in repolarization. The fact that the ghostburster was designed to contain only these three requirements, yet succeeds in producing burst discharge comparable to experiment, suggests that these three requirements capture the essential basis of the burst mechanism used in ELL pyramidal cells.

The simplicity of the ghostburster, as compared to the large compartmental model, has allowed us to understand, from a dynamical systems perspective, the mechanism involved in this type of bursting. The ghostburster was analyzed using a separation of the full dynamical system into fast and slow subspaces (Eq (7) and (8)), similar to the analysis of many other burst models (Rinzel, 1987; Rinzel and Ermentrout, 1989; Wang and Rinzel, 1995; Bertram et al., 1995; Hoppensteadt and Izhikevich, 1997; de Vries, 1998; Izhikevich, 2000; Golubitsky et al., 2001). Treating the slow dynamical variable p_d as a bifurcation parameter with respect to the fast subsystem allowed us to construct a 'burst shell' upon which the full burst dynamics evolve. The shell shows that a transition from a period-one limit cycle to a period-two limit cycle occurs in the dynamics of the fast subsystem as p_d is reduced. The period-two limit cycle causes a sharp reduction in $<V_d>$ since the second spike of the limit cycle is of reduced amplitude, due to dendritic refractoriness. The reduction in $<V_d>$ causes the $<V_d>(p_d)$ curve to cross the p_d nullcline, and p_d(t)grows during the second ISI of the period-two orbit. The growth in p_d(t) reinjects p_d(t) near a saddle-node bifurcation of fixed points occurring at high p_d. This passage near the 'ghost' of the saddle-node bifurcation causes the ISI to be long, separating the action potentials into bursts.

Recently, Izhikevich (2000) has approached the classification of bursters from a combinatorial point of view. This has been successful in producing a large number of new fast-slow bursting mechanisms. One of these burst mechanisms has been recently observed in a biophysically plausible model of bursting corticotroph cells of the pituitary (Shorten et al., 2000). In contrast, Golubitsky et al., (2001) (extending the work of Bertram et al. (1995), and de Vries (1998)) have classified bursters in terms of the unfoldings of high codimension bifurcations. Both these methods have used the implicit assumption that burst initiation and termination involve bifurcations from quiescence (or subthreshold oscillation) to limit-cycle and vice-versa. However, our burst mechanism does not appear in any of the above classifications. This is because, the trajectories in the fast subsystem of the ghostburster are always following a limit-cycle, and are never in 'true' quiescence, corresponding to a stable fixed point. The period of the limit cycle changes dynamically because the slow subsystem is oscillating, forcing the fast system to sometimes pass near the 'ghost' of an infinite period bifurcation. Furthermore, in the ghostburster, burst termination is connected with a bifurcation from a period-one to a period-two limit cycle in the fast subsystem. This is a novel concept, since burst termination in all other burst models is connected with a transition from a period-one limit cycle to a stable fixed point in the fast subsystem (Izhikevich 2000; Golubitsky et al., 2001). Thus, while classifying burst phenomena through the bifurcations from quiescence to a period-one limit cycle and vice-versa in the fast subsystem of a dynamical bursting model has had much success, our work requires an extension of the classification of bursting to include an alternative definition of 'quiescence' and a burst attractor which is composed of only period-one and period-two limit cycles with no stable fixed points.

Rinzel (1987) shows that burst mechanisms with a one-dimensional slow subsystem require bistability in the fast subsystem in order to exhibit bursting. The slow subsystem of ghostbuster equations is one dimensional, yet Figure 9 shows that the fast subsystem x is not bistable. This would seem to be a contradiction; however, recall that as τ_p approaches values that are similar to other bursting mechanisms, bursting is not observed. Thus our results do not contradict Rinzel's previous study, yet support a separate mechanism entirely. This illustrates a key distinction between the ghostburster and conventional bursting systems; the timescale of the slow variable has an upper bound in the ghostburster. The fast and slow timescales are sufficiently separate to allow us to successfully study the burst mechanism using a quasistatic approximation.

Thus ghostbursting, while distinct, does share similarities with conventional burst mechanisms. Note that mechanisms exist similar to ghostbursting, which involve a slow passage phenomena (requiring saddle-node or homoclinic bifurcations), may exist, placing the ghostburster as only one in a family of new burst mechanisms.

The ghostburster model exhibits a threshold between tonic firing and bursting behaviour. Both Terman (1991,1992) and Wang (1993) have also identified thresholds between these behaviours in the Hindmarsh-Rose model and a modified version of the Morris-Lecar equations, respectively. Both of these models exhibited a homoclinic orbit in the fast subsystem as the spiking phase of a burst terminated. As a result, the bifurcations from continuous spiking to busting in the full dynamics were complicated. Wang observed a crises bifurcation at the transition (Grebogi et al., 1983), whereas Terman showed that a series of bifurcations occurs during the transition, which could be shown to exhibit dynamics similar to the Smale horseshoe map (Guckenheimer and Holmes, 1983). The saddle-node bifurcation of limit cycles that separates the two regimes in the Ghostburster model is a great deal simpler than either of these bifurcations. However, interestingly Wang has shown that an intermittent route to chaos is also observed in the Hindmarsh-Rose model as continuous spiking transitions into bursting, much like the Ghostburster system.

The fact that the transition from tonic firing to bursting in the Ghostburster system occurs as depolarization is increased, is in contrast to both experimental and modeling results of other bursting cells (Terman 1992; Hayashi and Ishizuka, 1992; Wang 1993; Gray and McCormick, 1996; Steriade et al., 1998; Wang, 1999). However, since many experimental and modeling results, separate from ELL, show burst threshold behaviour, the concept of 'burst excitability' may have broader implications. To expand, the saddle-node bifurcation of limit cycles marking burst threshold can be compared to the saddle-node bifurcation of fixed points, which is connected to the spike excitability of Type I membranes (Ermentrout, 1996; Hoppensteadt and Izhikevich, 1997). The functional implication of a burst threshold have yet to be fully understood, however recent work suggests that it may have important implications for both the signaling of inputs (Eugia et al., 2000) and dividing cell response into stimulus estimation (tonic firing) and signal detection (bursting) (Sherman, 2001).

4.2 Predictions for bursting in the ELL

An integral part of the burst mechanism in ELL pyramidal cells is the interaction between the soma and dendrite through action potential backpropagation. One potential function of backpropagation is thought to be retrograde signaling to dendritic synapses (Häusser et al., 2000). Further, a recent experimental study has shown that the coincidence of action potential backpropagation and EPSPs produce a significant amplification in membrane potential depolarization (Stuart and Häusser, 2001). These results may have consequences for both synaptic plasticity and dendritic computation. Our results (and those of others, see Häusser et al., 2000 for a review) imply that backpropagation can also determine action potential patterning.

As mentioned above, the ghostburster exhibits a threshold separating tonic firing and bursting as depolarization is increased. Similar behaviour has been observed in both *in vitro* and *in vivo* experimental recordings of ELL pyramidal cells (Lemon and Turner, 2000; Bastian and Nguyenkim, 2001), and in our full compartmental model simulations (data not shown). A reduction of burst threshold was observed in ELL pyramidal cells when TEA (K^+ channel blocker) was focally applied to the proximal apical dendrite (Noonan et al., 2001; Rashid et al., 2001). Our work is consistent with this observation, since dendritic TEA application is equivalent to a reduction in $g_{Dr,d}$ conductance in our model. Figure 6 shows that as $g_{Dr,d}$ is reduced burst threshold is lowered.

Bursts, as opposed to individual spikes, have been suggested to be a fundamental unit of information (Lisman, 1997). In fact, Gabbiani et al., (1996) have correlated bursts from ELL pyramidal cells with features in the stimulus driving the cell. Considering these results, it is possible that the time scale of bursting, T ($= T_B + T_{IB}$), could be tuned to sensory input, hence the ability of a bursting cell to alter T may improve its coding efficiency. A natural method to alter T would be to change the time constant(s), τ, that determine the slow process of the burst mechanism (Giannakopoulous et al., 2000). Nevertheless, to achieve an order of magnitude change in T requires a potentially large change in τ. Recently, Booth and Bose (2001) have shown, in a two-compartmental model of a bursting CA3 pyramidal cell, that the precise timing of inhibitory synaptic potentials can change the burst period T. Their results have potential implications for the rate and temporal coding of hippocampal place cells. However, the ghostburster shows that both T_B and T_{IB} can be changed by an order of magnitude, but with only small changes in either depolarizing input and/or dendritic K^+ conductances (see Figure 13). Small changes in I_S are

conceivable through realistic modulations of feedforward and feedback input which occur during electro-location and electro-communication in weakly electric fish (Heiligenburg, 1991). Changes in $g_{Dr,d}$ can further occur through the phosphorylation of dendritic K^+ channels, such as *Apt*Kv3.3 which has been shown to be abundant over the whole dendritic tree of ELL pyramidal cells (Rashid et al., 2001). Hence, the ghostbursting mechanism may offer ELL pyramidal cells a viable method by which to optimize sensory coding with regulated burst output. Further studies, quantifying the information-theoretic relevance of bursting, are required to confirm these speculations.

We conclude our study with a concrete prediction. Figures 10,12, and 13 show that the full burst period T of ELL pyramidal cells can be significantly decreased as either depolarizing current (I_S) is increased or dendritic K^+ conductance ($g_{Dr,d}$) is decreased by a small amount. This prediction can be easily verified by experimentally measuring T in bursting ELL pyramidal cells for 1) step changes in I_S , and 2) before and after TEA application to the apical dendrites, which will change $g_{Dr,d}$. Modification of other ionic currents, persistent sodium and somatic K^+ in particular, may also be used to create similar bifurcation sets as in Figure 13.

5- Acknowledgements

We would like to thank our colleague Ray W. Turner for the generous use of his data and fruitful discussions. Valuable insight on the analysis of our model was provided by John Lewis, Kashayar Pakdaman, Eugene Izhikevich, Gerda DeVries, Maurice Chacron, and Egon Spengler. This research was supported by operating grants from NSERC (B.D., A.L.), the OPREA (C.L.), and CIHR (L.M.).

References

Adams WB (1985) Slow depolarization and hyperpolarizing currents which mediate bursting in an *Aplysia* neurone R15. J. Physiol. (Lond.) 360:51-68.

Aldrich R, Getting P, and Thomson S (1979) Mechanism of frequency-dependent broadening of molluscan neuron soma spikes. J. Physiol. (Lond.) 291: 531-544.

Bastian J, and Nguyenkim J (2001) Dendritic Modulation of Burst-Like Firing in Sensory Neurons J. Neurophysiol. 85: 10-22.

Berman NJ, and Maler L (1999) Neural architecture of the electrosensory lateral line lobe: adaptations for coincidence detection, a sensory searchlight and frequency-dependent adaptive filtering. J. Exp. Biol. 202: 1243-1253, 1999

Bertram R, Butte MJ, Kiemel T, and Sherman A (1995) Topological and phenomenological classification of bursting oscillations. Bull. Math. Biol. 57:413-439.

Bland BH, and Colom LV (1993) Extrinsic and intrinsic properties underlying oscillation and synchrony in limbic cortex. Prog. Neurobiol. 41: 157-208.

Booth V, and Bose A (2001) Neural Mechanisms for Generating Rate and Temporal Codes in Model CA3 Pyramidal Cells. J. Neurophysiol. 85: 2432-2445.

Bressloff PC (1995) Dynamics of a compartmental model integrate-and fire neuron with somatic potential reset. Physica D 80: 399-412.

Brumberg JC, Nowak LG, McCormick DA (2000) Ionic Mechanisms Underlying Repetitive High-Frequency Burst Firing in Supragranular Cortical Neurons. J. Neurosci. 20: 4829-4843.

Carpenter GA (1979) Bursting Phenomena in Excitable Membranes. SIAM J. Appl. Math 36:334-372.

Chay TR, and Rinzel J (1985) Bursting, beating, and chaos in an excitable membrane model. Biophys. J. 48: 815-827.

Connors BW, Gutnick MJ, and Prince DA (1982) Electrophysiological properties of neocortical neurons in vitro. J. Neurophysiol. 48: 1302-1320.

Connors BW, and Gutnick MJ (1990) Intrinsic firing patterns of diverse neocortical neurons. TINS 13: 99-104.

de Vries G (1998) Multiple Bifurcations in a Polynomial Model of Bursting Oscillations. J. Nonlinear Sci. 8: 281-316.

Doedel E (1981) A program for the automatic bifurcation analysis of autonomous systems. Congr. Nemer. 30: 265-484.

Doiron B, Longtin A, Berman NJ, and Maler L (2001a) Subtractive and divisive inhibition: effect of voltage-dependent inhibitory conductances and noise. Neural. Comp. 13:227-248.

Doiron B, Longtin A, Turner RW, and Maler L (2001b) Model of gamma frequency burst discharge generated by conditional backpropagation. J. Neurophysiol., In Press.

Eguia MC, Rabinovich MI, and Abarbanel HDI (2000) Information transmission and recovery in neural communication channels. Phys. Rev. E 62: 7111-7122.

Ermentrout B (1996) Type I Membranes, Phase Resetting Curves, and Synchrony. Neural Comp. 8: 979-1001.

Franceschetti S, Guateo E, Panzica F, Sancini G, Wanke E, and Avanzini A (1995) Ionic mechanism underlying burst firing in pyramidal neurons: intracellular study in rat sensorimotor cortex. Brain Res 696:127-139.

Gabbiani F, Metzner W, Wessel R, and Koch C (1996) From stimulus encoding to feature extraction in weakly electric fish. Nature 384:564-567.

Gabbiani F, and Metzner W (1999) Encoding and processing of sensory information in neuronal spike trains. J. Exp. Biol. 202: 1267-1279.

Grebogi E, Ott E, and Yorke, JA. (1983) Crises, sudden changes in chaotic attractors and transient chaos. Physica D. 7:181-200.

Giannakopoulos F, Hauptmann C, and Zapp A (2000). Bursting activity in a model of a neuron with recurrent synaptic feedback. Fields Institute Communications, 29.

Golubitsky M, Krešimir J, and Kaper TJ (2001). An unfolding theory approach to bursting in fast-slow systems, In: Festschrift dedicated to Floris Takens, Global Analysis of Dynamical Systems, pg.277-308.

Gray CM, and McCormick DA (1996) Chattering cells: superficial pyramidal neurons contributing to the generation of synchronous oscillations in the visual cortex. Science 274:109-113.

Guckenheimer J., and Holmes P (1993) Nonlinear Oscillations, Dynamical Systems, and Bifurcations of Vector Fields. Springer-Verlag.

Häusser M, Spruston N, Stuart G (2000) Diversity and Dynamics of Dendritic Signaling. Science 290: 739-744.

Hayashi H, and Izhizuka S (1992) Chaotic Nature of Bursting Discharges in the *Onchidium* Pacemaker Neuron. J.Theor. Biol. 156:269-291.

Heiligenburg W (1991) Neural Nets in Electric Fish. MIT Press, Cambridge, MA.

Hodgkin A, and Huxley A (1952) A quantitative description of membrane current and its application to conduction and excitation in nerve. J. Physiol. 117: 500-544.

Hoppensteadt FC, and Izhikevich EM (1997) Weakly Connected Neural Networks. Springer-Verlag, N.Y.

Izhikevich EM (2000). Neural Excitability, Spiking, and Bursting. Int. J. Bifurc. Chaos 10:1171-1269.

Jensen M, Azouz R, and Yaari Y (1996) Spike after-depolarization and burst generation in adult rat hippocampal CA1 pyramdial cells. J. Physiol. 492: 199-210.

Keener J., and Sneyd J (1998) Mathematical Physiology. Springer-Verlag, NY.

Kepecs A, and Wang X-J (2000) Analysis of complex bursting in cortical pyramidal neuron models. Neurocompt. 32-33:181-187.

Komendantov AO, and Kononenko NI (1996) Deterministic Chaos in Mathematical Model of Pacemaker Activity in Bursting Neurons of Snail, Helix Pomatia. J.Theor. Biol. 183:219-230.

Lánsky P, and Rodriguez R (1999) The spatial properties of a model neuron increase its coding range. Biol. Cybern. 81: 161-167.

Lemon N, and Turner RW (2000) Conditional spike backpropagation generates burst discharge in a sensory neuron. J. Neurophysiol. *84:1519-1530*.

Lisman JE (1997) Bursts as a unit of neural information: making unreliable synapses reliable. TINS 20: 28-43.

Ma M, and Koester J (1995) Consequences and mechanisms of spike broadening of R20 cells in *Aplysia Californica*. J. Neurosci. 15:6720-6734.

Mainen ZF, Joerges J, Huguenard JR, and Sejnowski TJ (1995) A model of spike initiation in neocortical pyramidal cells. Neuron 15: 1427-1439.

Mainen ZF, and Sejnowski TJ (1996) Influence of dendritic structure on firing pattern in model neocortical neurons. *Nature* 382:363-365.

McCormick DA, Connors BW, Lighthall JW, and Prince DA (1985) Comparative electrophysiology of pyramidal and sparsely spiny stellate neurons of the neocortex. J. Neurophysiol. 54: 782-806.

Metzner W, Koch C, Wessel R, and Gabbiani F (1998) Feature extraction of burst-like spike patterns in multiple sensory maps. J. Neurosci. 15:2283-2300.

Noonan LM, Morales E, Rashid AJ, Dunn R.J, and Turner RW (2000) Kv3.3 channels have multiple roles in regulating somatic and dendritic spike discharge. XXX Proc. Soc. Neurosci., 26(2): 1638.

Paré D, Shink E, Gaudreau H, Destexhe A, and Lang EJ (1998) Impact of spontaneous synaptic activity on the resting properties of cat neocortical neurons in vivo. J. Neurophysiol. 79: 1450-1460.

Pinault D, and Deschênes M (1992) Voltage-Dependent 40 Hz oscillations in rat reticular thalamic neurons *in vivo*, Neurosci., 51:245-258.

Pinsky P, and Rinzel, J (1994) Intrinsic and network rhythmogenesis in a reduced Traub model for CA3 neurons. J. Comput. Neurosci. 1, 39-60.

Pomeau Y, and Manneville P (1980) Intermittent Transition to Turbulence in Dissipative Dynamical Systems. Comm. Math. Phys. 74:189-197.

Rashid AJ, Morales E, Turner RW, and Dunn RJ (2001) Dendritic Kv3 K^+ channels regulate burst threshold in a sensory neuron. J. Neurosci. 21: 125-135.

Rinzel J (1987) A formal classification of bursting in excitable systems. In: Teramoto E. and Yamaguti M, eds. Mathematical Topics in Population Biology, Morphogenesis, and Neurosciences. Lecture Notes in Biomathematics. Vol. 71, Springer-Verlag, Berlin.

Rinzel J., and Ermentrout B (1989). Analysis of Neural Excitability and Oscillations. In: Koch C. and Segev I, eds. Methods in Neuronal Modeling. MIT Press, Cambridge MA, pg. 251-291.

Shao L-R, Halvorsrud R, Borg-Graham L, and Strom J (1999). The role of BK-type Ca^{2+} dependent K^+ channels in spike broadening during repetitive firing in rat hippocampal pyramidal cells. J. Physiol. (Lond.) 521: 135-146.

Sherman A, Carrol P, Santos RM, and Atwater I (1990) Glucose dose response of pancreatic beta-cells: Experimental and theoretical results. In : Hidalgo C eds. Transduction in Biological Systems, Plenum Press, NY, 1990.

Sherman SM (2001) Tonic and burst firing: dual modes of thalmocortical relay. TINS 24:122-127.

Shorten PR, and Wall, D (2000) A Hodgkin-Huxley Model Exhibiting Bursting Oscillations. Bull. Math. Biol. 62: 695-715.

Steriade M, McCormick DA , and Sejnowski TJ (1993). Thalamocortical oscillations in the sleeping and aroused brain. Science 262: 679-85.

Steriade M, Timofeev I, Dürmüller N, and Grenier F (1998) Dynamic properties of corticothalamic neurons and local cortical interneurons generating fast rhythmic (30-40 Hz) spike bursts. J. Neurophysiol. 79: 483-490.

Strogatz SH (1994) Nonlinear Dynamics and Chaos with Applications to Physics, Biology, Chemistry, and Engineering. Addison-Wesley, Reading, MA.

Stuart G, and Sakmann B (1994) Active propagation of somatic action potentials into neocortical pyramidal cell dendrites. Nature 367: 69-72.

Stuart G, Spruston N, Sakmann B, and Häusser M (1997) Action potential initiation and backpropagation in neurons of the mammalian CNS. TINS 20:125-131.

Terman D (1991) Chaotic spikes arising from a model of bursting in excitable membranes SIAM J. Appl. Math 51: 1418-1450.

Terman D (1992) The transition from bursting to continuous spiking in excitable membrane models. J. Nonlinear Sci. 2: 135-182.

Traub R, Wong R, Miles R, and Michelson H (1994). A model of a CA3 hippocampal neuron incorporating voltage-clamp data on intrinsic conductances. J. Neurophysiol. 66: 635-650.

Turner RW, Maler L, Deerinck T, Levinson SR, and Ellisman M (1994) TTX-sensitive dendritic sodium channels underlie oscillatory discharge in a vertebrate sensory neuron. J. Neurosci. 14: 6453-6471.

Turner RW, Plant J, and Maler L (1996) Oscillatory and burst discharge across electrosensory topographic maps. J. Neurophysiol. 76:2364-2382.

Turner RW, and Maler L (1999) Oscillatory and burst discharge in the apteronotid electrosensory lateral line lobe. J. Exp. Biol. 202:1255-1265.

Vetter P, Roth A, and Häusser M (2001) Propagation of action potentials in dendrites depends on dendritic morphology. J. Neurophysiol. 85:926-937.

Wang X-J (1993). Genesis of bursting oscillations in the Hindmarsh-Rose model and homoclinicity to a chaotic saddle. Physica D 62:263-274.

Wang X-J, and Rinzel J (1995). Oscillatory and bursting properties of neurons. In: ed. Arbib MA. The Handbook of Brain Theory and Neural Networks. Cambridge MA: MIT Press, pp. 686-691.

Wang X-J (1999) Fast burst firing and short-term synaptic plasticity: a model of neocortical chattering neurons. Neurosci. 89:347-362.

Figure Legends

FIG 1. ELL burst discharge and dendritic backpropagation. **A**. *In vitro* recording of burst discharge from the soma of an ELL pyramidal cell with constant applied depolarizing current. Two bursts of action potentials are shown, each exhibiting a growing depolarization as the burst evolves, causing the ISI to decrease; the burst ends with a high frequency doublet ISI. The doublet triggers a sharp removal of the depolarization, uncovering a prominent AHP, labeled a burst-AHP. **B**. Active Na^+ conductances are distributed along the soma and proximal apical dendrite of ELL pyramidal cells (left). Na^+ regions are indicated with vertical bars to the left of the schematic. Note that the distribution of dendritic Na^+ is punctuate, giving regions of high Na^+ concentration (often referred to as "hot spots") separated by regions of passive dendrite. The active dendritic regions allow for backpropagation of a somatic action potential through a dendritic action potential response, as seen from ELL recordings from both the soma and proximal (~ 150 μm) dendrite (right). Somatic action potential rectification by K^+ currents and the broader action potential in the dendrite allow for electrotonic conduction of the dendritic action potential to the soma, resulting in a DAP at the soma (bottom left). We thank R.W. Turner for generously providing his data for the figure.

FIG 2. Schematic of two-compartment model representation of an ELL pyramidal cell. The ionic currents that influence both the somatic and dendritic compartment potentials are indicated. Arrows which point into the compartment represent inward Na^+ currents, whereas arrows pointing outward represent K^+ currents (the specific currents are introduced in the text). The compartments are joined through an axial resistance, $1/g_c$, allowing current to be passed between the somatic and dendritic compartments.

FIG 3. Model bursting. **A**. Time series of the somatic potential V_s during burst output. **B**. Dendritic $I_{Dr,d}$ inactivation variable p_d during the same burst simulation as in A. Note the cumulative (slow) inactivation as the burst evolves and the rapid recovery from inactivation during the inter-burst period.

FIG 4. Model performance. A single burst is obtained from ELL pyramidal cell recordings (top row; data donated by R. W. Turner), full multi-compartmental model simulations (middle row; simulation presented in Doiron et al., 2001b), and reduced two-compartment model simulations (bottom row; eqs (1)-(6)). All bursts are produced by applying constant depolarization to the soma (0.3 nA top; 0.6 nA middle; I_s = 9, bottom). The columns show both somatic and dendritic responses for each row. The reduced model somatic spike train reproduces both the *in vitro* data and full model simulation spike trains by showing the growth of DAPs and reduction in ISI as the burst evolves. All somatic bursts are terminated with a large bAHP, which is connected to the dendritic spike failure.

FIG 5. **A**. Bifurcation diagram of the ghostburster equations (Eqs (1)-(6)) as a function of the bifurcation parameter I_S. We choose h_d as the representative dynamic variable and plot h_d on the vertical axis. For $I_S < I_{S1}$ a stable fixed point (solid line) and a saddle (dashed line) coexist. A saddle-node bifurcation of fixed points (SNFP) occurs at $I_S = I_{S1}$. For $I_{S1} < I_S < I_{S2}$ stable (filled circles) and unstable (open circles) limit cycles coexist, the maximum and minimum of which are plotted. A saddle-node bifurcation of limit cycles (SNLC) occurs at $I_S = I_{S2}$. For $I_S > I_{S2}$ a chaotic attractor exists; we show this by plotting the maximum and minimum of h_d for all ISIs that occur in a 1s simulation for fixed I_S. A reverse period doubling cascade out of chaos is observed for large I_S. The software package AUTO (Doedel, 1981) was used to construct the leftmost part of the diagram. Chaotic states are shown by plotting the minimum and maximum of h_d for each ISI of a 1000 ms spike train. **B**. Instantaneous frequency (1/ISI) is plotted for 1000 ms simulations of the ghostburster model for each increment in I_S. The transitions from rest to tonic firing and tonic firing to chaotic bursting are clear. **C.** The maximum Lyapunov exponent λ as a function of I_S.

FIG 6. Two parameter bifurcation set. Both the saddle-node bifurcations of fixed points (SNFP) and limit cycles (SNLC) bifurcations were tracked, using AUTO (Doedel 1981) in the (I_S , $g_{Dr,d}$) subspace of parameter space. The curves partition the space into quiescence, tonic firing, and chaotic bursting regimes.

FIG 7. **A**. Quasistatic bifurcation diagram. p_d is fixed as a bifurcation parameter while V_d is chosen as a representative variable from the fast subsystem x. The maxima in the dendritic voltage ($\frac{dV_d}{dt} = 0$ and $\frac{d^2V_d}{dt^2} < 0$) are plotted for each value of p_d. At $p_d = p_{d1}$ the maxima of V_d switch to two values, corresponding to the values taken during each ISI of a period-two solution. **B**. Time series of the dendritic voltage, V_d(t), while $p_d = 0.13 > p_{d1}$. The fast subsystem follows a period-one solution. **C**. Time series of the dendritic voltage, V_d(t), while $p_d = 0.08 < p_{d1}$. The fast subsystem follows a period-two solution. A constant value of $I_S = 9 > I_{S1}$ is chosen for all simulations in *A*,*B*, and *C*.

FIG 8. p_d(t) and $\tilde{p}_d$ computed from integration of the ghostburster equations with I_S=9 > I_{S2}. Four bursts are shown with the corresponding time stamped spikes given above for reference. A Slow

burst oscillation in p_d(t) is observed. It is evident that the discrete function $\tilde{p}_d$ (solid circles) tracks the burst oscillation in p_d(t). $\tilde{p}_d$ shows a monotonic decrease throughout the burst until the inter-burst interval, at which point $\tilde{p}_d$ is reinjected to a higher value. The horizontal lines are the values p_{d1}, corresponding to the period doubling transition, and p_{d2}, corresponding to the crossing of the nullcline curve with the $<V_d>$ curve. The p_d(t) reinjection occurs after $p_d(t)<p_{d2}$ as explained in the text. $\tilde{p}_d$ has been translated downward to lie on top of the p_d(t) time series. This is required because Eq (10) uses a unweighted average of V_d, given in Eq (9). This produces a $\tilde{p}_d$ series which occurs at higher values than p_d(t) because Eq (9) and (10) ignore the low pass characteristics of Eq (6). However, only the shape of $\tilde{p}_d$ is of interest and this is not affected by the downward translation.

FIG 9. **A**. The bifurcation diagram of Figure 6*A* is re-plotted along with the p_d nullcline $p_{d,\infty}(V_d)$ (dashed line labeled *N*). Note that the p_d nullcline is inverted so as to give $V_{d,\infty}(p_d) = V_{1/2,p} - k_p \ln(1/1-p_d)$. We plot the average of V_d over a whole period of V_d,$<V_d>$ (solid line), at a fixed p_d. Note the sharp decline in $<V_d>$ for p_d below p_{d1}. **B**. The diagram in 9*A* is re-plotted with the labels removed. A single directed burst trajectory projected in the (V_d,p_d) plane obtained by integrating the full dynamical system (Eqs (1)-(6)) is plotted on top of the 'burst shell'. **C**. All observed discharge frequencies of the fast subsystem are plotted as a function of p_d. At $p_d = p_{d1}$ a stable period-one firing pattern of ~ 200 Hz changes to a period-two solution with one ISI being ~ $(700\ \text{Hz})^{-1}$ and the other ~ $(100\text{Hz})^{-1}$. The inverse of the ISIs of the single burst shown in Figure 9B are plotted as well. The ISIs are numbered from 1 (the first ISI) through to 5 (doublet ISI) and 6 (inter-burst interval). **D**. The average of the derivative of p_d, $\left\langle dp_d/dt \right\rangle$, is plotted for each ISI in the single burst shown in Figure 8*B*. Only the long inter-burst ISI has $\left\langle dp_d/dt \right\rangle > 0$,all other ISIs have $\left\langle dp_d/dt \right\rangle < 0$. A constant value of $I_S = 9 > I_{S1}$ is chosen for all simulations in *A*, *B*, *C*, and *D*.

FIG 10. Inter-burst interval. $<T_{IB}>$ is plotted as a function of $I_S - I_{S1}$. The averaging was performed on 100 bursts produced by the ghostburster equations at a specific I_S. $g_{Dr,d}$ was set to 12.14. $<T_{IB}>$ shows a similar functional form to that described by Eq (11). The dips in $<T_{IB}>$ are discussed in the text.

FIG 11. Burst intermittency. ***A***. The ISI return map for a single burst sequence with I_S=6.587 and $g_{Dr,d}$=13 is shown (for these parameters I_{S1}=5.736 and I_{S2}=6.5775). The diagonal is plotted as well (dashed line). The labels (1)-(5) are explained in the text. ***B*.** The ISI return map for a single burst sequence with I_S=9 and $g_{Dr,d}$=15 as in Figure 3. ***C***. The ISI return map for a single burst recording from an ELL pyramidal cell (Data courtesy of R.W. Turner). Compare with the model burst sequence in *B*.

FIG 12. Burst interval $<T_B>$ plotted as a function of $I_S - I_{S2}$. The averaging was performed on 100 bursts produced by the ghostburster equations at a specific I_S. $g_{Dr,d}$ was set to 12.14. $<T_B>$ shows a similar functional form to that described by Eq (12).

FIG 13. Burst Gallery. **A**. Reproduction of the two parameter bifurcation set shown in Figure 6. The letters *B-F* marked inside the Figure correspond to the (I_S, $g_{Dr,d}$) parameter values used to produce panels *B-F* respectively. Examples of the inter-burst period T_{IB} and burst period T_B for each burst train are indicated (except for the tonic solution shown in *B*). The exact I_S and $g_{Dr,d}$ values used to produce each spike train are as follows: **B**. I_S=6.5, $g_{Dr,d}$=14 **C**. I_S= 7.7, $g_{Dr,d}$=13; **D**. I_S=7.6, $g_{Dr,d}$=14; **E**. I_S=5.748, $g_{Dr,d}$=12.14; **F**. I_S=5.75, $g_{Dr,d}$=11. The vertical mV scale bar in *C* applies to all panels, however, each panel has its own horizontal time scale bar.

Table I

Current	$\mathbf{g_{max}}$	$\mathbf{V_{1/2}}$	**K**	**t**
$I_{Na,s}(m_{\infty,s}(V_s))$	55	-40	3	N/A
$I_{Dr,s}(n_s(V_s))$	20	-40	3	0.39
$I_{Na,d}(m_{\infty,d}(V_d)/h_d(V_d))$	5	-40/-52	5/-5	N/A /1
$I_{Dr,d}(n_d(V_d)/p_d(V_d))$	15	-40/-65	5/-6	0.9/5

TABLE I. Model parameter values. The values correspond to the parameters introduced in eq (1)-(6). Each ionic current ($I_{Na,s}$; $I_{Dr,s}$; $I_{Na,d}$; $I_{Dr,d}$) is modeled by a maximal conductance g_{max} (in units of mS/cm^2), sigmoidal activation, and possibly inactivation, infinite conductance curves involving both $V_{1/2}$ and k parameters $m_{\infty,s}(V_s) = 1/(1+e^{-(V_s-V_{1/2})/k})$, and a channel time constant τ (in units of ms). Double entries x/y correspond to channels with both activation (x) and inactivation (y) respectively. If the activation time constant value is N/A then the channel activation tracks the membrane potential instantaneously. Other parameters values are; g_c = 1, κ = 0.4, V_{Na} = 40 mV, V_K = -88.5 mV, V_{leak} = -70 mV, g_{leak} = 0.18, and C_m=1 μF/cm^2. These values compare in magnitude to those of other two-compartment models (Pinsky and Rinzel, 1994; Mainen and Sejnowski, 1995).

Fig1

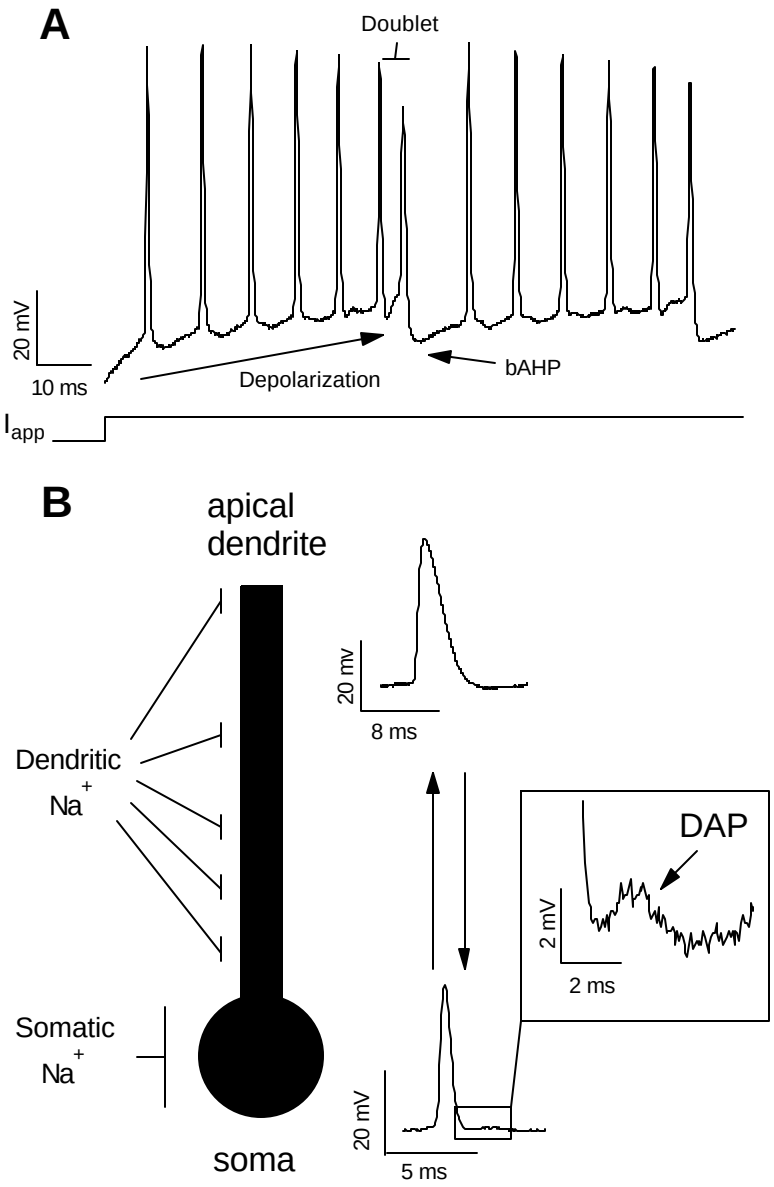
A
Doublet
20 mV
10 ms
Depolarization
bAHP
I app
B
apical dendrite
20 mv
8 ms
Dendritic Na+
DAP
2 mV
2 ms
Somatic Na+
20 mV
5 ms
soma

Fig2

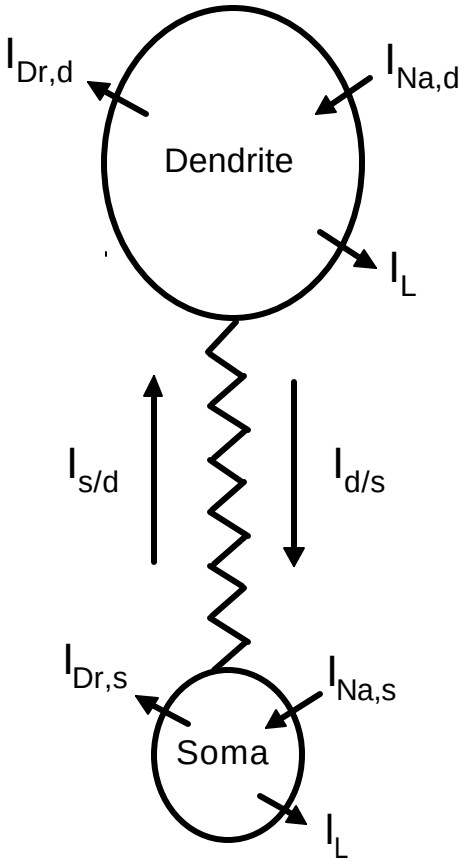

Fig3

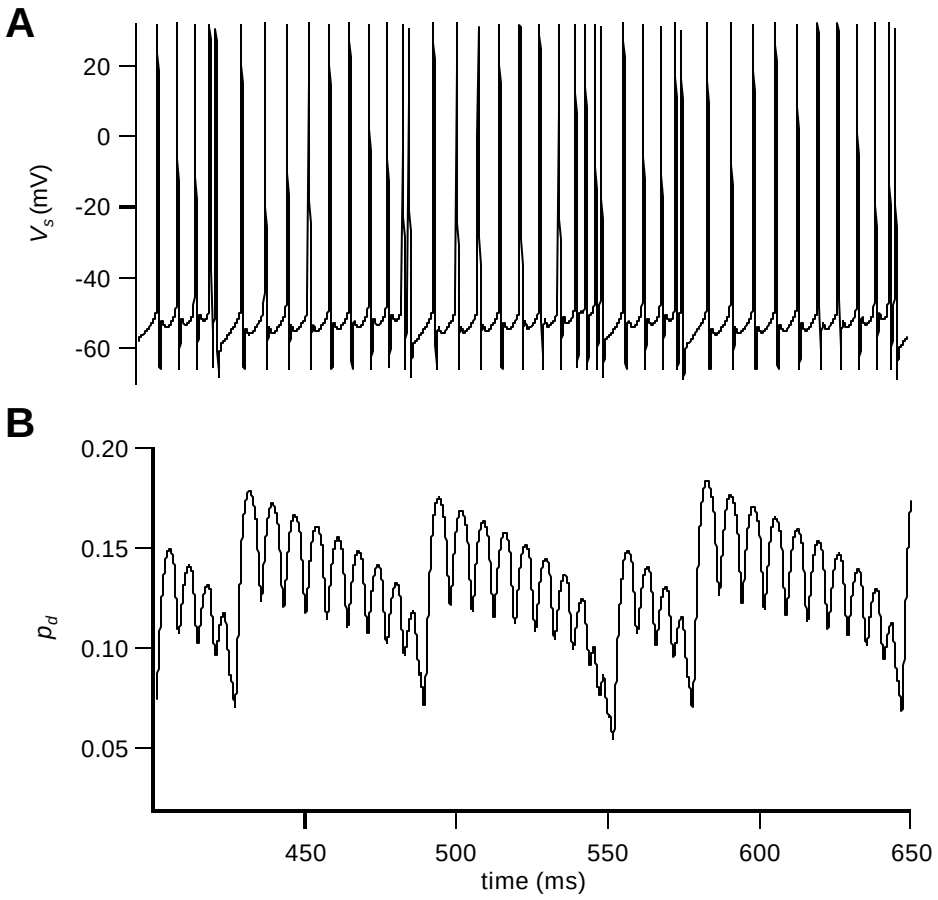
A
20
0
-20
-40
-60
V_s (mV)
B
0.20
0.15
0.10
0.05
p_d
450
500
550
600
650
time (ms)

Fig4

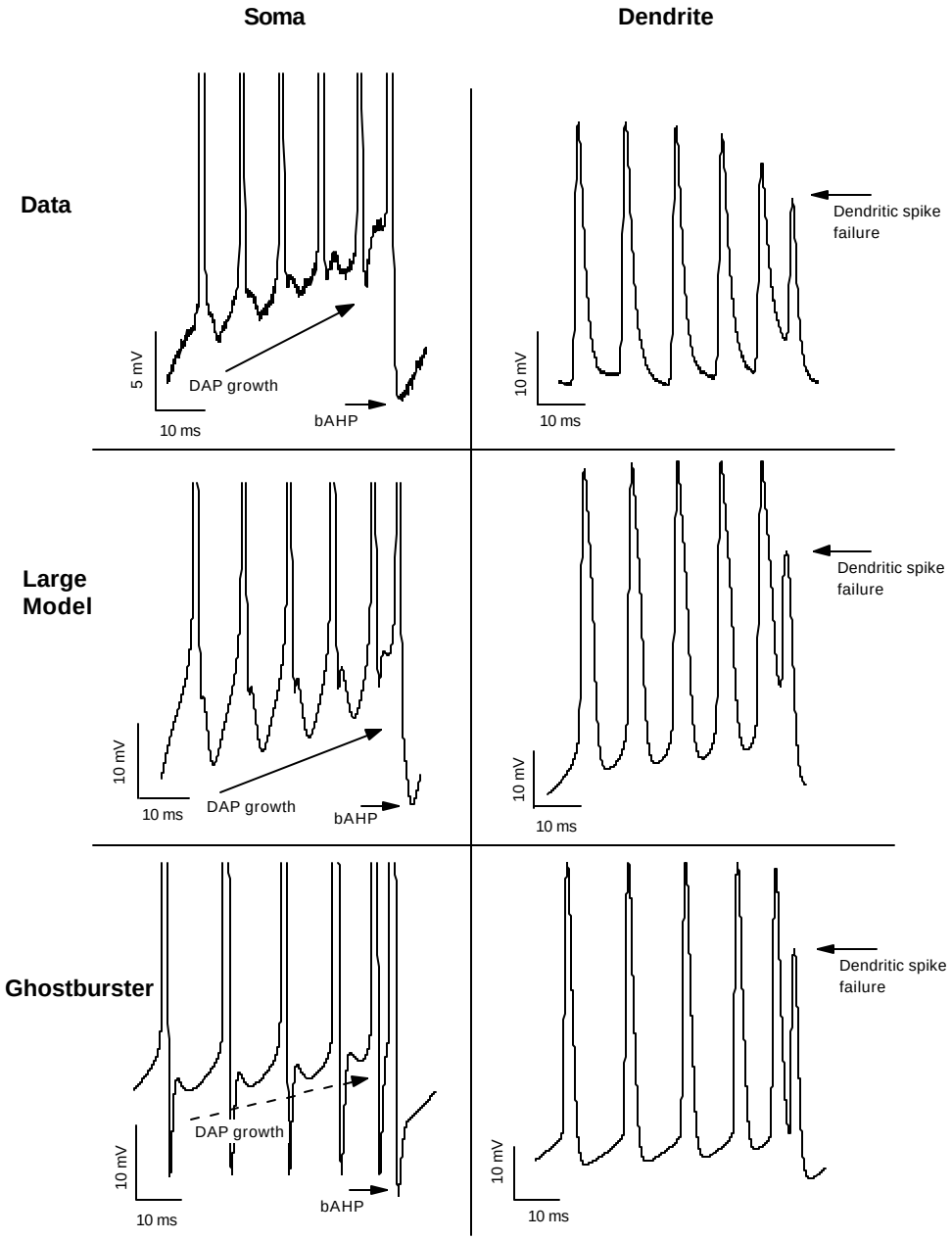
Soma
Dendrite
Data
Large Model
Ghostburster
5 mV
10 mV
10 ms
DAP growth
bAHP
Dendritic spike failure

Fig5

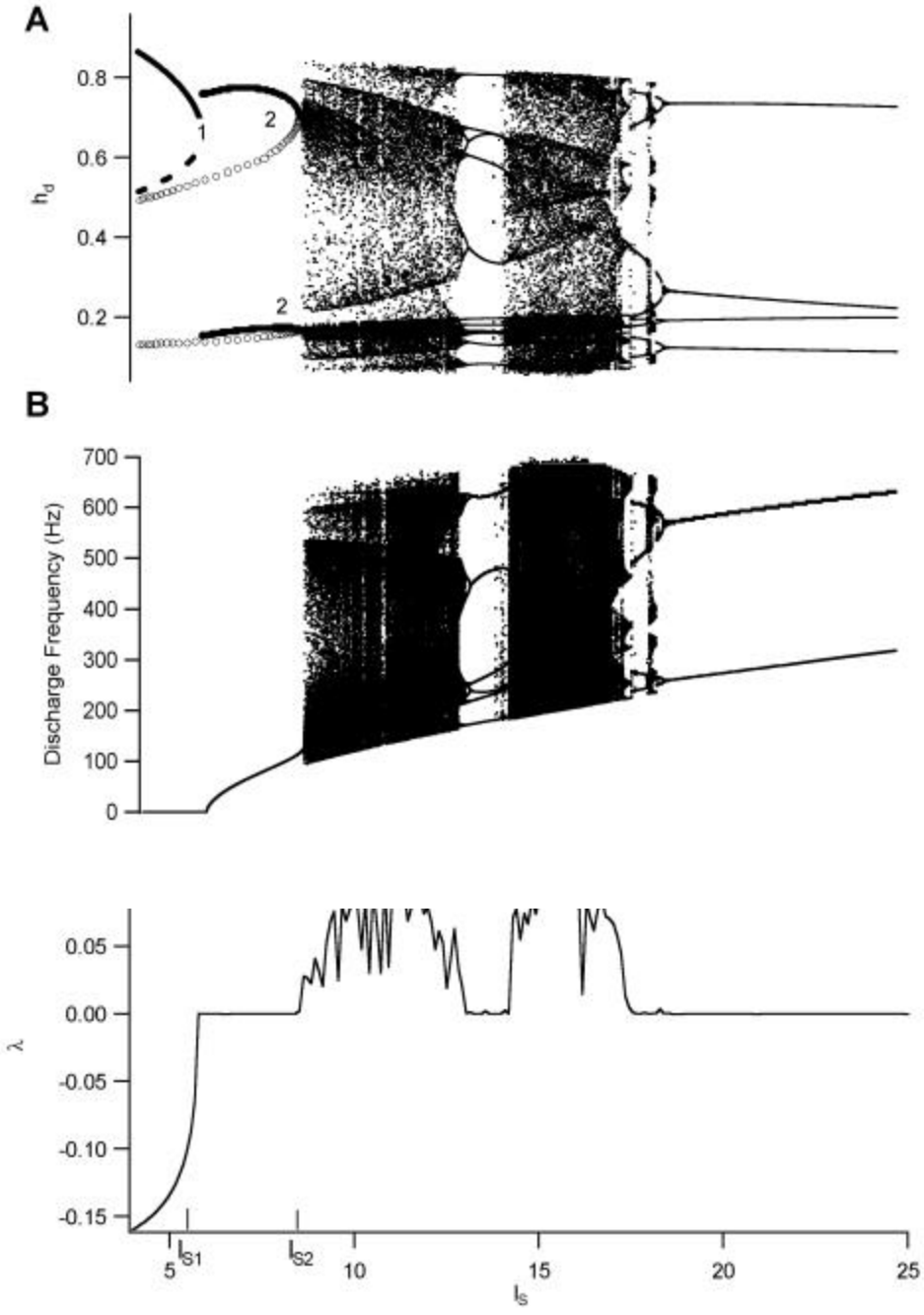
A
0.8
0.6
0.4
0.2
h_d
1
2
2
B
Discharge Frequency (Hz)
700
600
500
400
300
200
100
0
0.05
0.00
-0.05
-0.10
-0.15
λ
I_{S1}
I_{S2}
5
10
15
20
25
I_S

Fig6

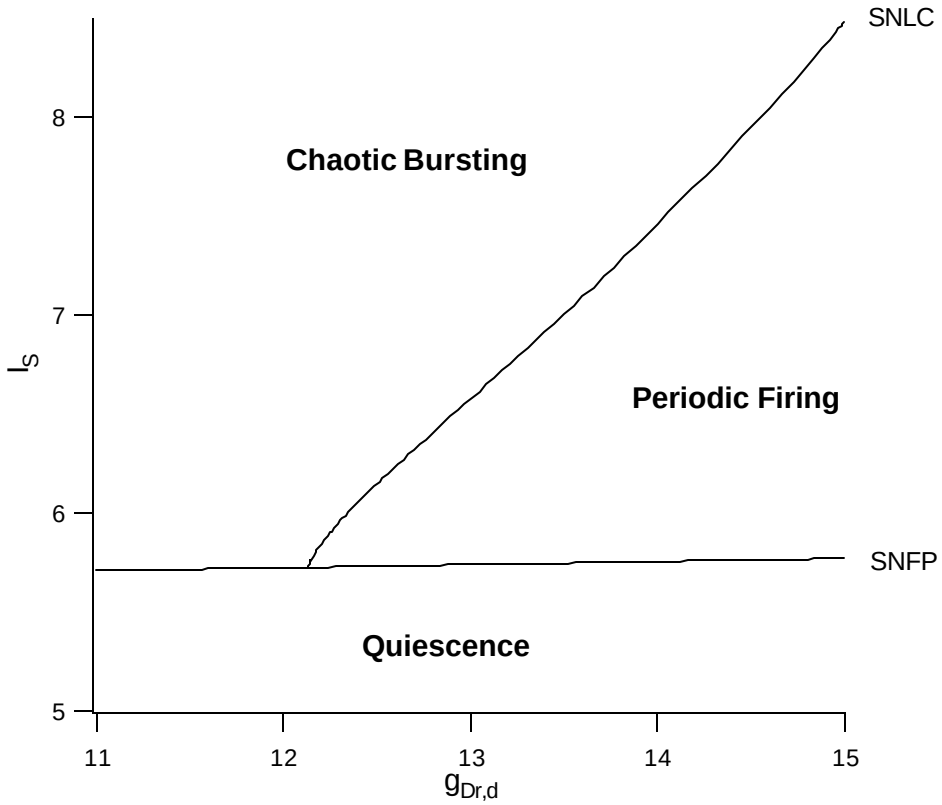
SNLC
8
Chaotic Bursting
7
I_S
Periodic Firing
6
SNFP
Quiescence
5
11
12
13
14
15
$g_{Dr,d}$

Fig7

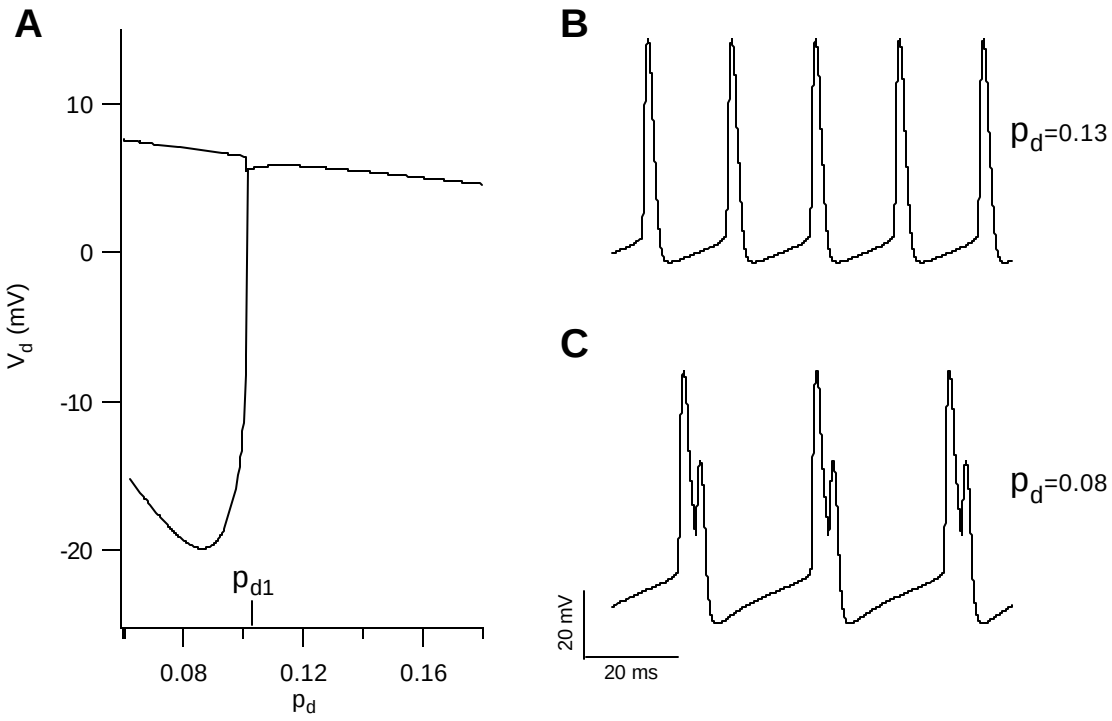

Fig8

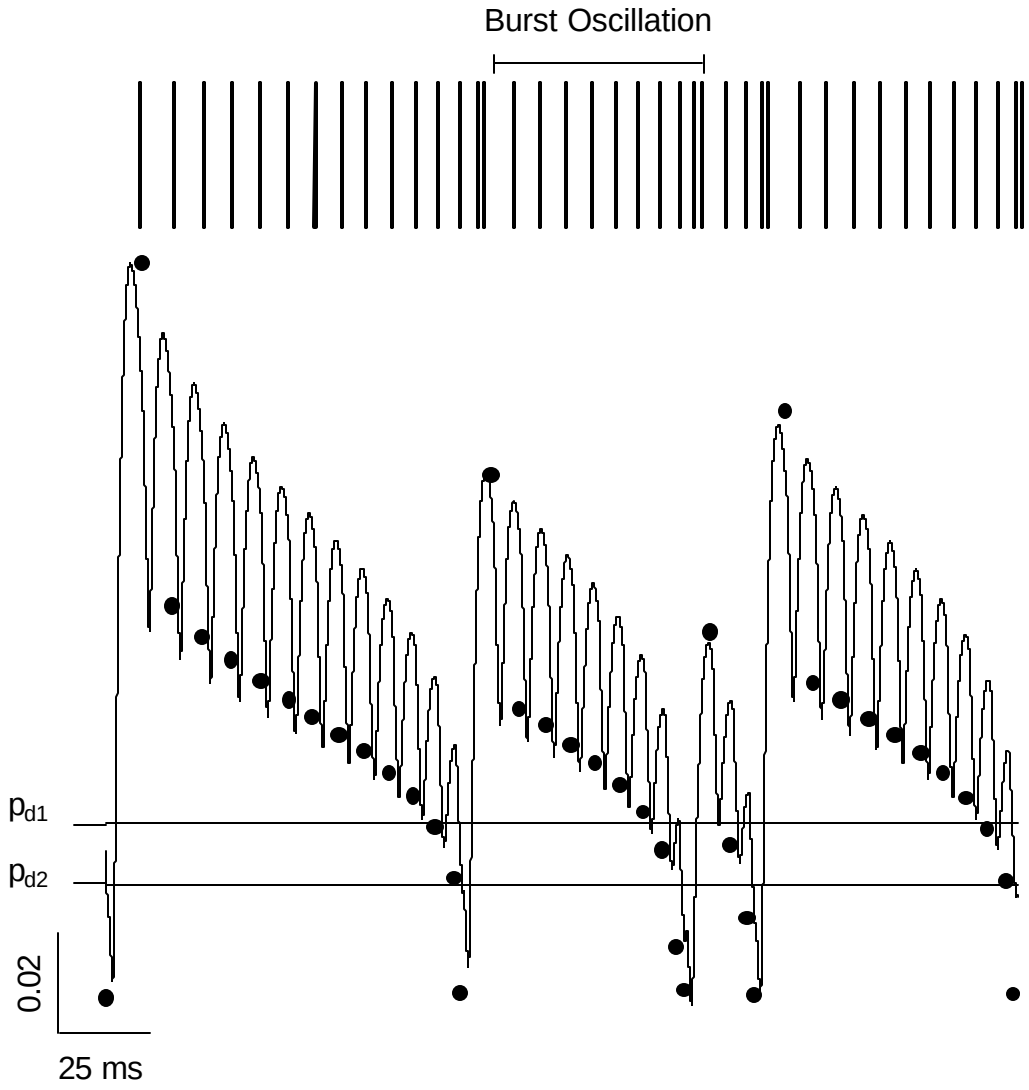

Fig9

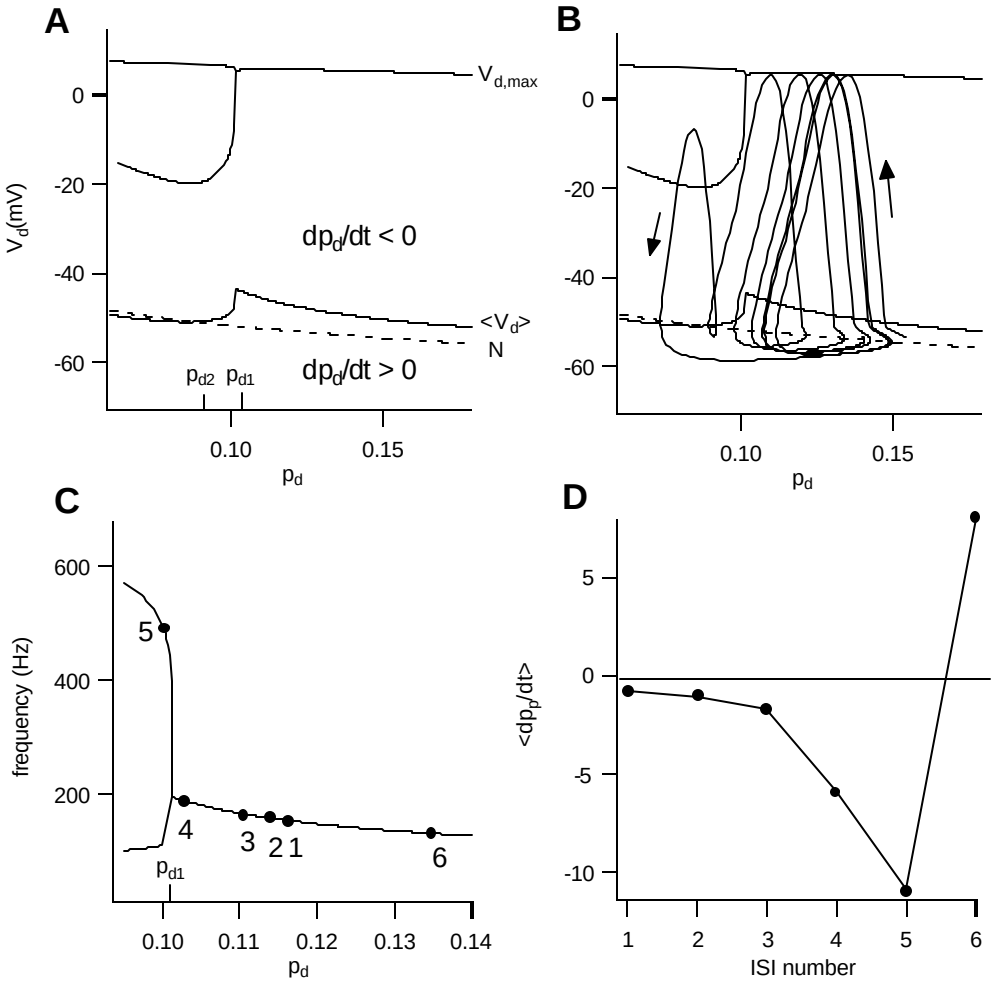
A
B
C
D
$V_{d,max}$
$dp_d/dt < 0$
$<V_d>$
N
$dp_d/dt > 0$
p_{d2} p_{d1}
V_d(mV)
p_d
frequency (Hz)
$<dp_d/dt>$
ISI number
1 2 3 4 5 6

Fig10

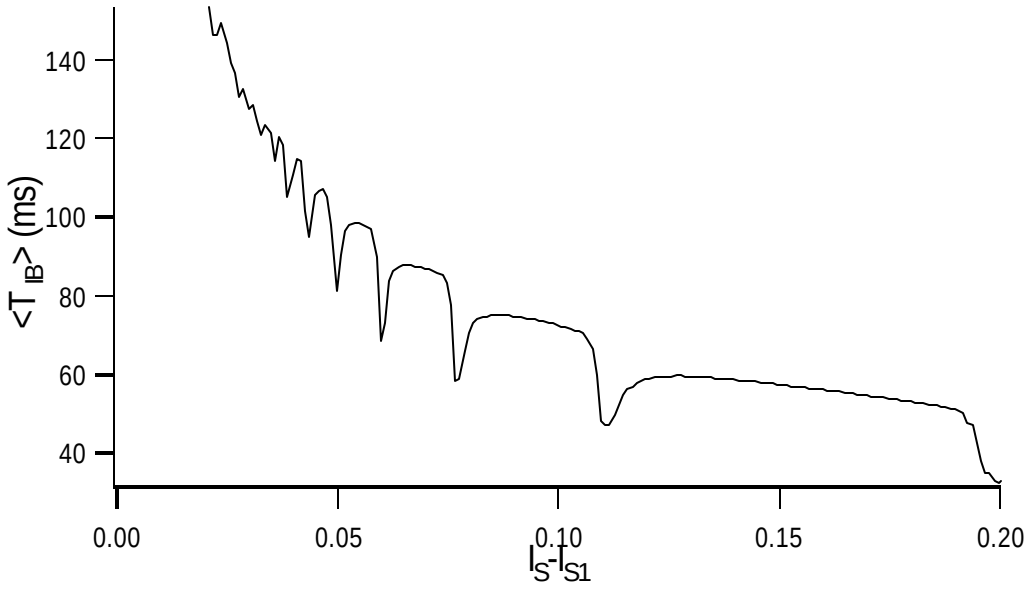

Fig11

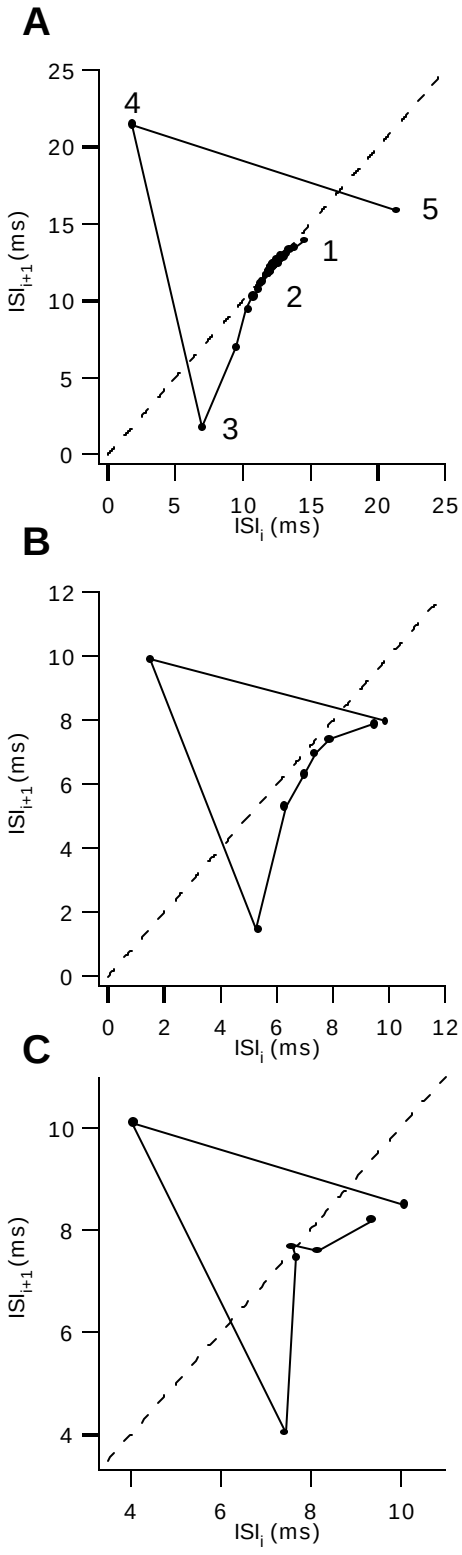

Fig12

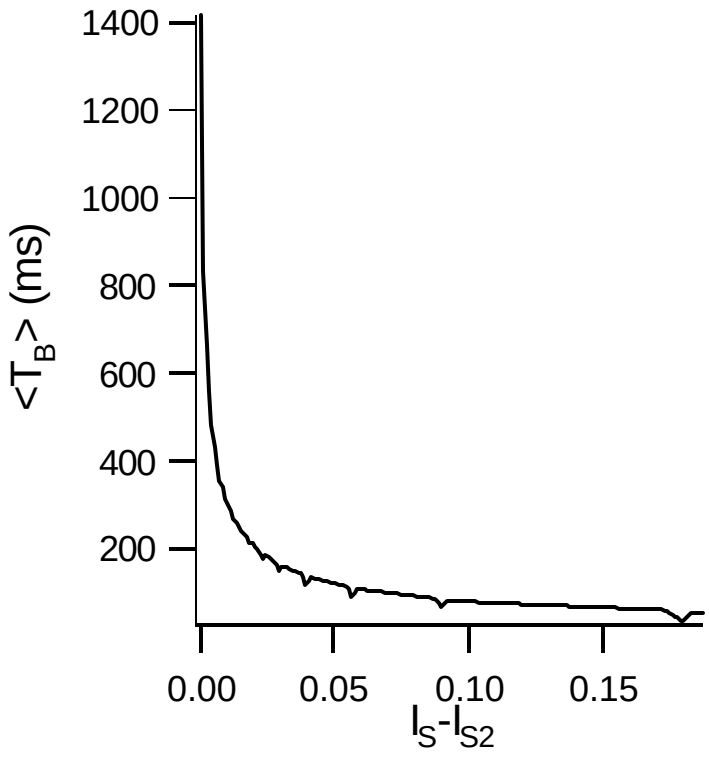

Fig13

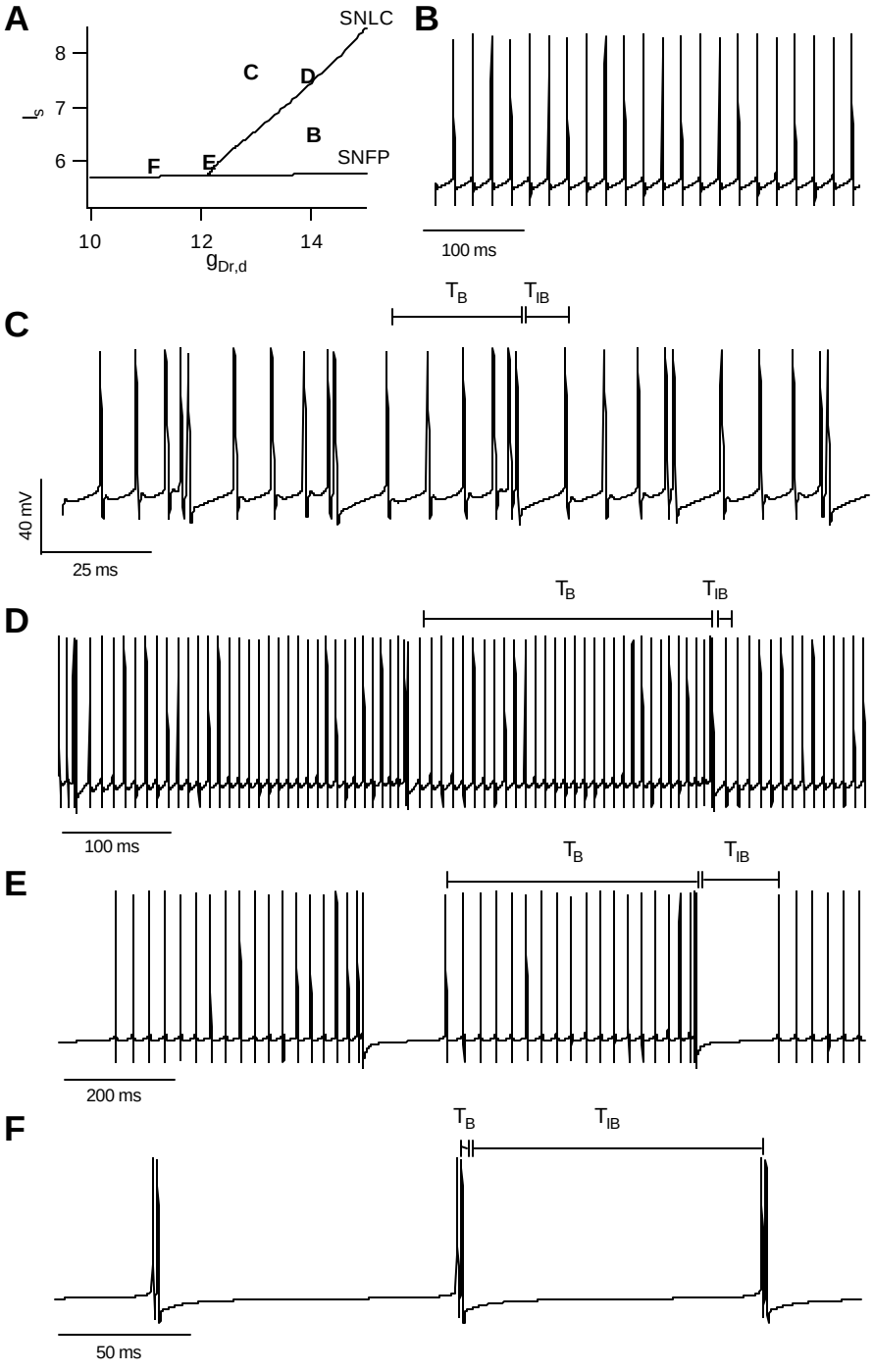
A
SNLC
8
7
6
I_s
C
D
B
F
E
SNFP
10
12
14
$g_{Dr,d}$
B
100 ms
C
T_B
T_{IB}
40 mV
25 ms
D
T_B
T_{IB}
100 ms
E
T_B
T_{IB}
200 ms
F
T_B
T_{IB}
50 ms